COMETARY ORIGIN OF THE ZODIACAL CLOUD AND CARBONACEOUS MICROMETEORITES. IMPLICATIONS FOR HOT DEBRIS DISKS

2010 ApJ 713 816

(http://iopscience.iop.org/0004-637X/713/2/816)

The Astrophysical Journal, 713:816–836, 2010 April 20 doi:10.1088/0004-637X/713/2/816

COMETARY ORIGIN OF THE ZODIACAL CLOUD AND CARBONACEOUS MICROMETEORITES. IMPLICATIONS FOR HOT DEBRIS DISKS

David Nesvorný[1,2], Peter Jenniskens[3], Harold F. Levison[1,2], William F. Bottke[1,2], David Vokrouhlický[4], and Matthieu Gounelle[5]

[1] Department of Space Studies, Southwest Research Institute, 1050 Walnut St., Suite 400, Boulder, CO 80302, USA
[2] Center for Lunar Origin & Evolution, NASA Lunar Science Institute, Boulder, CO 80302, USA
[3] Carl Sagan Center, SETI Institute, 515 N. Whisman Road, Mountain View, CA 94043, USA
[4] Institute of Astronomy, Charles University, V Holešovičkách 2, 180 00 Prague 8, Czech Republic
[5] Museum National d'Histoire Naturelle, Laboratoire de Minéralogie et Cosmochimie du Muséum, 61 rue Buffon, 75005 Paris, France
Received 2009 October 26; accepted 2010 February 28; published 2010 March 26

ABSTRACT

The zodiacal cloud is a thick circumsolar disk of small debris particles produced by asteroid collisions and comets. Their relative contribution and how particles of different sizes dynamically evolve to produce the observed phenomena of light scattering, thermal emission, and meteoroid impacts are unknown. Until now, zodiacal cloud models have been phenomenological in nature, composed of ad hoc components with properties not understood from basic physical processes. Here, we present a zodiacal cloud model based on the orbital properties and lifetimes of comets and asteroids, and on the dynamical evolution of dust after ejection. The model is quantitatively constrained by *Infrared Astronomical Satellite* (*IRAS*) observations of thermal emission, but also qualitatively consistent with other zodiacal cloud observations, with meteor observations, with spacecraft impact experiments, and with properties of recovered micrometeorites (MMs). We find that particles produced by Jupiter-family comets (JFCs) are scattered by Jupiter before they are able to orbitally decouple from the planet and drift down to 1 AU. Therefore, the inclination distribution of JFC particles is broader than that of their source comets and leads to good fits to the broad latitudinal distribution of fluxes observed by *IRAS*. We find that 85%–95% of the observed mid-infrared emission is produced by particles from JFCs and <10% by dust from long-period comets. The JFC particles that contribute to the observed cross section area of the zodiacal cloud are typically $D \approx 100$ μm in diameter. Asteroidal dust is found to be present at <10%. We suggest that spontaneous disruptions of JFCs, rather than the usual cometary activity driven by sublimating volatiles, is the main mechanism that liberates cometary particles into the zodiacal cloud. The ejected mm to cm-sized particles, which may constitute the basic grain size in comets, are disrupted on $\lesssim$10,000 yr to produce the 10–1000 μm grains that dominate the thermal emission and mass influx. Breakup products with $D > 100$ μm undergo a further collisional cascade with smaller fragments being progressively more affected by Poynting–Robertson (PR) drag. Upon reaching $D < 100$ μm, the particles typically drift down to <1 AU without suffering further disruptions. The resulting Earth-impact speed and direction of JFC particles is a strong function of particle size. While 300 μm to 1 mm sporadic meteoroids are still on eccentric JFC-like orbits and impact from antihelion/helion directions, which is consistent with the aperture radar observations, the 10–300 μm particles have their orbits circularized by PR drag, impact at low speeds, and are not detected by radar. Our results imply that JFC particles represent ~85% of the total mass influx at Earth. Since their atmospheric entry speeds are typically low ($\approx$14.5 km s^{-1} mean for $D = 100$–200 μm with $\approx$12 km s^{-1} being the most common case), many JFC grains should survive frictional heating and land on Earth's surface. This explains why most MMs collected in antarctic ice have primitive carbonaceous composition. The present mass of the inner zodiacal cloud at <5 AU is estimated to be 1–2 $\times 10^{19}$ g, mainly in $D = 100$–200 μm particles. The inner zodiacal cloud should have been $>10^4$ times brighter during the Late Heavy Bombardment (LHB) epoch $\approx$3.8 Gyr ago, when the outer planets scattered numerous comets into the inner solar system. The bright debris disks with a large 24 μm excess observed around mature stars may be an indication of massive cometary populations existing in those systems. We estimate that at least $\sim 10^{22}$, $\sim 2 \times 10^{21}$, and $\sim 2 \times 10^{20}$ g of primitive dark dust material could have been accreted during LHB by the Earth, Mars, and Moon, respectively.

Key words: comets: general – minor planets, asteroids: general – zodiacal dust

1. INTRODUCTION

The zodiacal cloud is a dynamic assembly of meteoroids in bound orbits around the Sun. The orbits depend on particle size, location in the cloud, and the type of parent body. Interstellar dust particles that pass through the solar system are not considered in this paper, nor are small meteoroid fragments that move out of the solar system on hyperbolic orbits ("beta-meteoroids").

Traditionally, the zodiacal cloud has been described with phenomenological models of dust distributions to explain the amount of scattered light (Hong 1985; Kniessel & Mann 1991; Ishiguro et al. 1999; Hahn et al. 2002), the Doppler shifts of the solar Mg I Fraunhofer line (Hirschi & Beard 1987; Mukai & Mann 1993; Clarke et al. 1996; Reynolds et al. 2004), and the more easily to interpret thermal emission observed in various lines of sight (Kelsall et al. 1998; Maris et al. 2006). Particularly good scattered light observations came from the Clementine mission (Hahn et al. 2002), while thermal infrared observations are mostly from the *Infrared Astronomical Satellite* (*IRAS*; Low et al. 1984; Hauser et al. 1984; Good et al. 1986; Sykes 1990), the *Cosmic Background Explorer* (*COBE*; Reach et al. 1995;

Kelsall et al. 1998), the *Midcourse Space Experiment* (*MSX*; Price et al. 2003), the *Infrared Space Observatory* (*ISO*; Fixsen & Dwek 2002; Leinert et al. 2002; Reach et al. 2003; Mueller et al. 2005), and the *Spitzer Space Telescope* (Bhattacharya & Reach 2004; Reach et al. 2007).

The phenomenological models successfully describe the size, spatial and velocity distributions of dust particles in the solar system (e.g., Grün et al. 1985; Divine 1993; Dikarev et al. 2004). They are particularly useful for accessing the satellite impact hazard, designing spacecraft impact experiments and studies of extrasolar emission sources such as the cosmic microwave background (e.g., Kelsall et al. 1998). The phemenological models, however, fall short in answering basic questions related to the origin of the zodiacal cloud, its temporal brightness variability, and the provenance of interplanetary particles collected at the Earth. Consequently, the origin of the zodiacal cloud, interplanetary dust particles (IDPs) collected in Earth's stratosphere (e.g., Love & Brownlee 1993), and micrometeorites (MMs) on the ground (Taylor et al. 1996; Engrand & Maurette 1998; Farley et al. 1998, 2006; Genge 2006) is still a matter of considerable debate. This limits our ability to link the detailed laboratory studies of IDPs and MMs to the properties of their parent bodies, and to use the zodiacal cloud as a valuable reference for studies of the exozodiacal debris disks.

Detailed dynamical models can be more useful in this context. At the root of dynamical models are the physical properties of interplanetary dust, such as density, geometric albedo, elemental composition, mineralogy, tensile strength, heat capacity, etc. (e.g., Dumont & Levasseur-Regourd 1988; McDonnell & Gardner 1998; Gustafson 1994; Gustafson et al. 2001; Levasseur-Regourd et al. 2001), which determine the behavior of particles in interplanetary space (e.g., planetary perturbations, collisions, sublimation, sputtering) and their interaction with a detector (e.g., ablation of MMs in Earth's atmosphere, ^{3}He retention, thermal radiation, light scattering). In dynamical models, the individual particles are tracked by numerical codes as they evolve by various processes from their sources (assumed to be, e.g., asteroids, comets, satellites or Kuiper Belt objects) to sinks (e.g., when they sublimate, disrupt, impact or leave the solar system). Insights into the origin of the zodiacal cloud can be obtained by calibrating the results of dynamical models on observations.

Until now, detailed dynamical models have been only developed for asteroidal dust to explain the origin of the zodiacal dust bands (e.g., Dermott et al. 1984; Grogan et al. 1997, 2001; Reach et al. 1997; Nesvorný et al. 2006; Vokrouhlický et al. 2008) and trapped dust in Earth's Langrange points first seen in *IRAS* observations (Dermott et al. 1994b). It has been established that the dust bands originate from the youngest asteroid families (Nesvorný et al. 2003, 2008). However, claims that asteroids are a major if not dominant source of zodiacal dust, by assuming that all main belt asteroids contribute dust (e.g., Dermott et al. 1995; Durda & Dermott 1997; Kortenkamp & Dermott 1998), have remained in doubt.

Models of the zodiacal cloud need not only explain line-of-sight properties, but also the observed influx of meteors (see Ceplecha et al. 1998; Jenniskens 2006, for a review) and the impact rate of meteoroids on satellites (Love & Brownlee 1993). Until now, models that were developed to explain these dynamical phenomena (e.g., Grün et al. 1985; Divine 1993; Staubach et al. 1997; Dikarev et al. 2004) were based on ad hoc populations of meteoroids in various types of orbits without a dynamical underpinning to sources and sinks. Moreover, all current satellite impact models use meteoroid velocity distributions (both magnitude and spatial direction) derived from meteor observations (Taylor & Elford 1998; Jones & Brown 1993; Brown & Jones 1999; Brown & Campbell-Brown 2003), which pertain to much bigger particles than typically encountered by satellites.

In this paper, we investigate what fraction of the zodiacal cloud is due to cometary versus asteroidal dust by calculating the evolution of dust particles under solar radiation forces and planetary perturbations (including resonances and close encounters), ejected from model populations of all potential sources (not just representative examples). The source populations include asteroids, active and mostly dormant Jupiter-family comets (JFCs), Halley-type comets (HTCs), and long-period Oort-cloud comets (OCCs). In recent years, much insight was gained into the dynamical characteristics of these populations and the number of asteroids and comets that can contribute dust to the zodiacal cloud (e.g., Levison & Duncan 1994, 1997; Jedicke & Metcalfe 1998; Wiegert & Tremaine 1999; Dones et al. 2004; Francis 2005; Gladman et al. 2009). At the same time, it was realized that mostly dormant JFCs are the main source of meteoroid streams in the inner solar system (Jenniskens 2006, 2008) and responsible for the antihelion/helion sources in the sporadic meteoroid background (Jenniskens 2006; Wiegert et al. 2009).

Here, we couple these new insights to dynamical behavior of cometary and asteroidal dust in order to evaluate the contribution of various sources to the thermal emission of zodiacal dust and the influx of MMs. We show that JFCs are the main source of zodiacal dust inside 5 AU and the most likely source of the MMs found on Earth. Our results also provide quantitative constraints on dust lifetimes, influx rates, and velocity distributions directly from the known abundances of meteoroid parent bodies. The results are used to quantify the properties of zodiacal dust cloud in the past and discuss implications for studies of exozodiacal debris disks.

To set up the stage for our modeling described in Section 3, we discuss *IRAS* observations of the zodiacal cloud in Section 2. Results are presented in Section 4. In Section 5, we estimate the current and historical terrestrial accretion rates of dust and discuss the implications of our work for studies of MMs and debris disks. Comet disruptions/splitting events are reviewed in Section 6. We suggest that they are the main mechanism by which the cometary particles are liberated from their parent bodies into the zodiacal cloud. The mass-loss rate from JFCs must be large enough to supply the IDP complex against losses (Lisse 2002). Previous work and origin of dust particles beyond Jupiter are discussed in Sections 7 and 8, respectively.

2. CONSTRAINTS

Our primary constraints are the observations of the zodiacal cloud by *IRAS* which have been confirmed by *COBE* and *Spitzer* (Hauser et al. 1984; Low et al. 1984; Kelsall et al. 1998; Sykes et al. 2004). *IRAS* measured mid-infrared (MIR) fluxes in four filters with effective wavelengths of 12, 25, 60, and 100 μm. These filters can be used as windows into the dust distribution at different distances from the Sun. Measurements in the 12 μm *IRAS* band are mainly sensitive to distributions of particles at $\sim$1–2 AU, while the 25 and 60 μm band measurements preferentially detect thermal emission from larger distances. *IRAS* observations in the 100 μm band are less useful for probing the thermal radiation of dust particles in the inner solar system.

IRAS showed that the MIR brightness of the zodiacal cloud peaks at the ecliptic and has broad wings that extend all the way

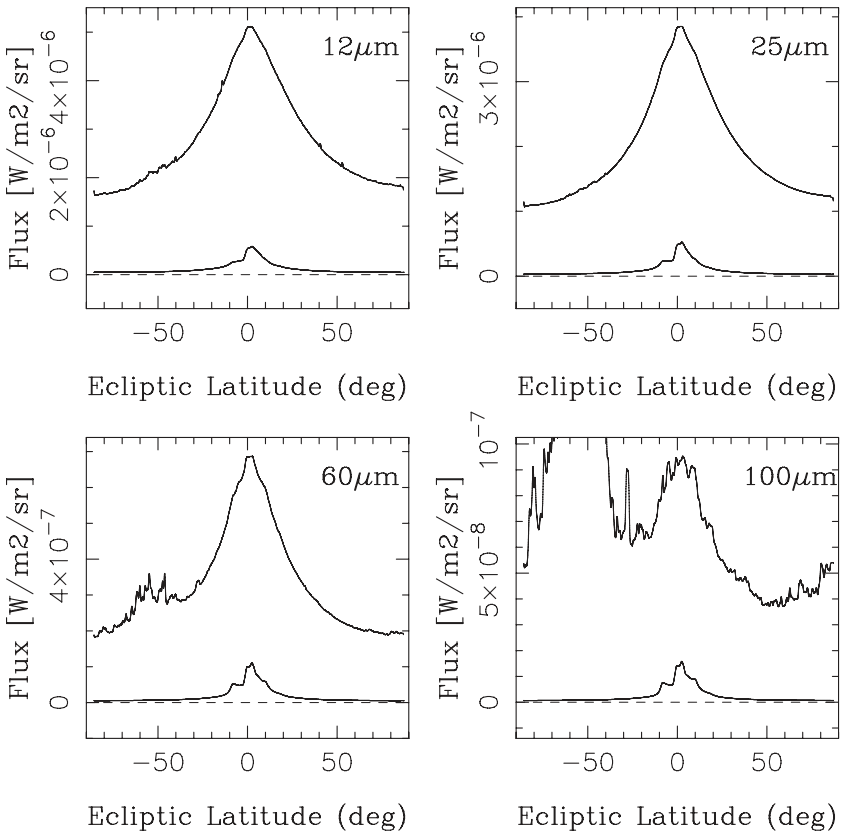

Figure 1. Upper solid lines in each panel show *IRAS* scan 180_24 (see Table 3 in NVBS06) that has been smoothed by a low-pass filter to remove point sources and instrumental noise. Different panels show fluxes at 12, 25, 60, and 100 μm *IRAS* wavelengths. The bottom solid lines show the contribution of three main asteroid dust bands to the observed fluxes. According to NVBS06, these dust bands contribute to the observed fluxes by ≈9%–15% within 10° to the ecliptic, and <5% overall. The strong signal at 100 μm between latitudes $b \approx -80°$ and $b \approx -30°$ is the galactic plane emission (also apparent at 60 μm). Figure from NVBS06.

to the ecliptic poles (Figure 1). The variation with the ecliptic longitude is minimal indicating that the zodiacal cloud is a nearly symmetrical disk of circumsolar particles that is roughly centered at the Sun (e.g., Staubach et al. 2001). The significant flux received from the ecliptic poles (∼1/3–1/4 of the ecliptic flux) also suggests that the cloud must be rather thick in the normal direction to the ecliptic plane.

Following Nesvorný et al. (2006, hereafter NVBS06), we selected several representative *IRAS* scans that met the following conditions. (1) We used scans that covered a continuous range of ecliptic latitudes from $b < -80°$ to $b > 80°$. (2) We did not use scans that had gaps created when the telescope skipped over bright sources. (3) We did not use scans that showed strong emission from extrasolar sources such as the galactic plane, galactic cirrus, point sources, etc. (4) We required that the selected scans covered all values of ecliptic longitude and the available range of solar elongations, $l_\odot$. Tables 2 and 3 in NVBS06 list the basic information about the selected scans.

In this work, we only consider scans with $l_\odot \approx 90°$. This is mainly done because the detail variation of brightness with $l_\odot$ is difficult to characterize as it requires an appropriate model for the collisional disruption of particles (NVBS06). We do not include the effects of collisions between particles in our model (except in Section 4.2, where a simple model for collisions is used). The considered value of $l_\odot$ is in the middle of the available range and thus best represents *IRAS* observations.

The zodiacal cloud is known to be warped and have a center that is slightly offset from the Sun. These features are produced by gravitational perturbations from Jupiter (Dermott et al. 1995, 2001). Since we are not interested in these detailed features of the zodiacal cloud here, we removed them by combining the selected *IRAS* scans into a representative profile. This was done by first shifting the scans by a small value in latitude (<2°), so that the peak of emission was centered exactly at $b = 0$, and calculating the average flux from all selected scans as a function of b. We ended up with profiles showing the mean fluxes at 12, 25, and 60 μm wavelengths as a function of ecliptic latitude (Figure 2). These profiles represent the main constraints on the work described here. Additional constraints are discussed in Section 4.3.

3. MODEL

Our model of the zodiacal cloud has four parts: we (1) define the initial orbital distributions of particles for different sources (asteroid and comet populations), (2) track the orbital evolution of particles with various sizes from sources to sinks, (3) determine the thermal infrared emission from these synthetic particle distributions, and (4) model the detection of their emission by *IRAS*. These model components are described below.

To simplify things, we do not initially account for the collisional disruptions of dust particles in the model. This is a major assumption which we verify in Section 4.2. For example, NVBS06 showed how the collisional disruption of particles, and production of smaller daughter products, affect the spatial distribution of particle populations in the asteroidal dust bands.

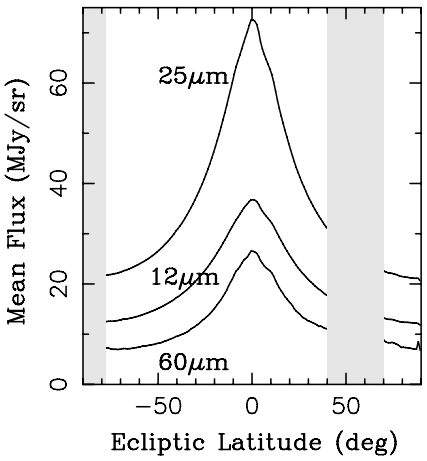

Figure 2. Mean *IRAS* profiles at 12, 25, and 60 μm wavelengths. To make these profiles, the selected *IRAS* scans were centered at the ecliptic, smoothed by a low-pass filter, and combined together. The gray rectangles at $l < -78^\circ$ and $40^\circ < l < 70^\circ$ block the latitude range where the mean fluxes were significantly affected by the galactic plane emission. We do not use the excluded range in this work. The uncertainties of the mean flux values are not shown here for clarity; they are too small to clearly appear in the plot. The characteristic errors at different wavelengths averaged over latitudes are $\sigma_{12\mu m} = 0.59$ MJy sr^{-1}, $\sigma_{25\mu m} = 1.1$ MJy sr^{-1}, and $\sigma_{60\mu m} = 2.7$ MJy sr^{-1}. They increase with wavelength due to the larger role of galactic emission at longer wavelengths.

The work described here, however, is less sensitive to collisional processes because the overall gross shape of the zodiacal cloud should be mainly controlled by the orbital distribution of its source population(s), violent dynamics of particles moving on planet-crossing orbits, and the effects of Poynting–Robertson (PR) drag. These features/processes are included in our model as we describe below.

3.1. Sources

Our model starts with the source population of objects. This may be either of the following: (1) individual asteroid groups such as the Karin, Veritas, or Beagle asteroid families (NVBS06; Nesvorný et al. 2008), (2) asteroid belt as a whole, (3) active JFCs defined by their debiased orbital distribution obtained from Levison & Duncan (1997, hereafter LD97) and their physical lifetime, (4) JFCs with orbital distribution similar to (3) but dynamically evolved beyond their nominal active lifespan, (5) HTCs, and (6) OCCs. These source populations are described in a more detail below.

We ignore the contribution of interstellar dust particles because thermal emission from these small particles (diameter $D < 1$ μm) would create diagnostic spectral features in the MIR wavelengths that are not observed (e.g., Reach et al. 2003). More specifically, observations of the MIR spectrum of the zodiacal cloud by Reach et al. (2003) suggest that the bulk of the zodiacal cloud is produced by ~10–100 μm particles. We also ignore dust produced by disruptive collisions in the Kuiper Belt (hereafter KB dust) because Landgraf et al. (2002) and Moro-Martín & Malhotra (2003) showed that KB dust particles should represent only a minor contribution to the inner zodiacal cloud.

Results for (1) were taken from NVBS06 and Nesvorný et al. (2008) who found that the three main dust bands discovered by Low et al. (1984) originate from the Karin, Veritas, and Beagle asteroid families. According to these results (Figure 1), the three main dust bands represent only ≈9%–15% of the zodiacal cloud emission at the ecliptic and <5% overall. About a dozen other dust bands have been identified (Sykes 1990). Since these dust bands are much fainter than the three main dust bands, Nesvorný et al. results set the upper limit on the contribution of *identified* asteroid breakups to the zodiacal cloud.

The orbital distribution of the asteroid belt source (2) is modeled by using the observed orbital distribution of asteroids with $D > 15$ km. We obtained this distribution from the ASTORB catalog (Bowell et al. 1994). This sample should be complete and unbiased (Jedicke & Metcalfe 1998; Gladman et al. 2009). The orbital distribution of asteroids with $D < 15$ km, which may be a better proxy for the initial distribution of dust produced in main belt collisions (Sykes & Greenberg 1986), is roughly similar to that of large asteroids. Thus, the orbital distribution that we use should be a reasonable assumption for (2).

The orbital distributions obtained by numerical integrations of test particle trajectories from individual comets would suffer from the heavily biased comet catalogs. Moreover, there are hundreds of known comets, each producing dust at a variable and typically unknown rate. In addition, it is also possible that the present zodiacal dust complex contains particles from lost parents as suggested by the orphaned Type-II trails (Sykes 1990) and identification of meteoroid streams with disrupted JFCs (see Jenniskens (2008) for a review). In view of these difficulties, we resorted to the following strategy.

The orbital distribution of JFCs was taken from LD97 who followed the evolution of bodies originating in the Kuiper Belt as they are scattered by planets and evolve in small fractions into the inner solar system. Starting at the time when the comets' perihelion distance, q, first drops below 2.5 AU in the LD97 simulations, we include it as an active JFC in our list of source objects. LD97 showed that the orbital distribution of visible JFCs obtained in this way nicely approximates the observed distribution. Moreover, LD97 argued that the inclination distribution of new JFCs (reaching $q < 2.5$ AU for the first time) is relatively narrow. The inclination distribution widens at later times as the JFC orbits become more spread by Jupiter encounters.

By comparing the width of the model inclination distribution with that of the observed JFCs, LD97 were able to estimate the fading lifetime of JFCs, $t_{\rm JFC}$, defined as the characteristic time between their first and last apparitions. They found that $t_{\rm JFC} = 12{,}000$ yr with a 90% confidence interval $3000 < t_{\rm JFC} < 30{,}000$ yr. See Figure 3 for an illustration of the steady-state JFC orbit distribution for $t_{\rm JFC} = 12{,}000$ yr. This is our initial distribution of particles produced by *active* JFCs. We use $t_{\rm JFC}$ as a free parameter in our model with values extending to $t_{\rm JFC} = 100{,}000$ yr to account for the possibility that an important dust component may be produced by old dormant JFCs as they spontaneously disrupt.

Our models for the orbital distributions of HTCs and OCCs are simpler than the one described for JFCs above, because we do not have in hand an appropriate numerical model that we could use with confidence. Fortunately, this is not a major limitation factor in this work because our main results described in Section 4 are not sensitive to the detailed properties of the HTCs and OCCs populations.

For HTCs, we assume that the differential distribution of the perihelion distance, $dN(q)$, is $dN(q) \propto q\,dq$, and set an upper limit of q at 3 AU. HTCs typically become visible/active only if they reach $q < 3$ AU. Similarly, the cumulative semimajor axis distribution of HTCs, $N(< a)$, is assumed to be $N(< a) \propto a$ with an upper cut on a at 50 AU. The differential inclination distribution $dN(i)$ is taken from Levison et al. (2006). This

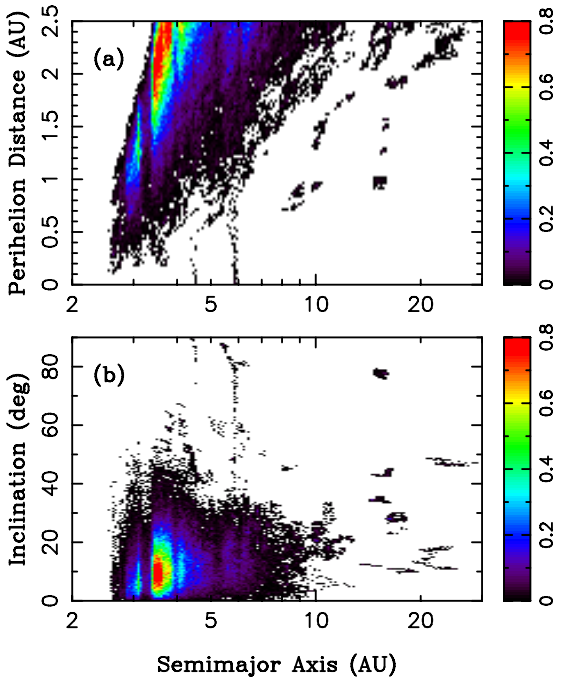

Figure 3. Orbital distribution of JFCs from the LD97 model. Panels show the perihelion distance (a), and inclination (b), as functions of the semimajor axis for JFCs with $q < 2.5$ AU and $t_{\rm JFC} = 12,000$ yr. See Section 3.1 for the definition of $t_{\rm JFC}$. The 2:1 and 3:2 mean-motion resonances with Jupiter correspond to the gaps in the distribution at $a \approx 3.3$ and 3.96 AU, respectively. The inclination distribution of JFCs shown here is remarkably similar to that obtained by Di Sisto et al. (2009; their Figure 10).

distribution can be approximately described by

$$dN(i) \propto \sin(i) e^{-\frac{1}{2}\left(\frac{i}{\sigma}\right)^2} di \qquad (1)$$

with $\sigma = 30^\circ$.

According to Francis (2005), the long-period comets have $dN(q) \propto (1 + \sqrt{q})\, dq$ for $q < 2$ AU. For $q > 2$ AU, Francis' study predicts $dN(q)$ being flat or declining while we would expect the perihelion distribution to increase with q. It probably just shows that the distribution is not well constrained for $q > 2$ AU. We use $dN(q) \propto 2.41(q/2)^\gamma\, dq$ for $q > 2$ AU with $0 < \gamma \leqslant 1$. The semimajor axis values of OCCs are set between 10,000 and 50,000 AU, which is known as the Oort spike (Wiegert & Tremaine 1999). We also use $a = 1000$ AU to check on the dynamical behavior of dust particles launched from the returning OCCs. The inclination distribution of OCCs is set to be uniformly random between 0° and 180°.

We tested two different methods to launch particles from their source objects. In the first method, chosen to approximate the ejection of particles from active comets, we launched particles at the perihelion when the mean anomaly $M = 0$. In the second method, we launched particles along the orbit with uniform distribution in M. This second method is more appropriate for the asteroidal particles and for particles produced by comet disruptions. Indeed, the identified comet disruptions do not seem to be correlated in any way with the perihelion passage (e.g., Weissman 1980). The two ejection methods produced comparable results. Given that disruptions should represent the main mass loss in comets (see Section 6), we use the second method for all results presented in Section 4. To simplify things, we neglect the ejection velocities of dust particles from their parent object and assume that they initially follow the parent object's orbit modified by the radiation pressure.

The individual comets in our model are assumed to contribute in roughly the same proportion to the circumsolar dust complex. The reasoning behind this assumption is that if an individual super-comet were the dominant source of circumsolar dust, the zodiacal cloud would not have such a smooth and symmetrical structure. In fact, the observed smooth structure of the zodiacal cloud probably implies a source population that contains numerous objects that are well mixed in the orbital space.

3.2. Orbit Evolution

The orbits of particles were tracked using the Wisdom–Holman map (Wisdom & Holman 1991) modified to include effects of radiation forces (Burns et al. 1979; Bertotti et al. 2003). The acceleration $\vec{F}$ on a particle due to these forces is

$$\vec{F} = \beta G \frac{m_\odot}{R^2} \left[\left(1 - \frac{\dot{R}}{c}\right) \frac{\vec{R}}{R} - \frac{\vec{V}}{c} \right], \qquad (2)$$

where $\vec{R}$ is the orbital radius vector of the particle, $\vec{V}$ is its velocity, G is the gravitational constant, $m_\odot$ is the mass of the Sun, c is the speed of light, and $\dot{R} = dR/dt$. The acceleration (2) consists of the radiation pressure and velocity-dependent PR terms. Parameter β is related to the radiation pressure coefficient, $Q_{\rm pr}$, by

$$\beta = 5.7 \times 10^{-5} \frac{Q_{\rm pr}}{\rho s}, \qquad (3)$$

where radius s and density ρ of the particle are in cgs units. Pressure coefficient $Q_{\rm pr}$ can be determined using the Mie theory (Burns et al. 1979). We used $Q_{\rm pr} = 1$ which corresponds to the geometrical optics limit where s is much larger than the incident-light wavelength. We assumed that the solar-wind drag force has the same functional form as the PR term and contributes by 30% to the total drag intensity (Gustafson 1994).

We used particles with diameter $D = 2s = 10$, 30, 100, 200, 300, 1000 μm and set their bulk density to $\rho = 2$ g cm^{-3}. For comparison, Love et al. (1994) reported $\rho \approx 2$ g cm^{-3} for stratospheric-collected IDPs, while McDonnell & Gardner (1998) found mean $\rho = 2$–2.4 g cm^{-3} from the analysis of data collected by the LDEF and Eureca satellites. On the other hand, density of 1 g cm^{-3} has been often assumed for cometary matter (e.g., Joswiak et al. 2007; Wiegert et al. 2009). Grün et al. (1985) suggested that 20%–40% of particles may have low densities whereas most meteoroids have $\rho = 2$–3 g cm^{-3}. Our results may be easily rescaled to any ρ value and we explicitly discuss the effect of ρ wherever it is appropriate.

The particle orbits were numerically integrated with the `swift_rmvs3` code (Levison & Duncan 1994) which is an efficient implementation of the Wisdom–Holman map and which, in addition, can deal with close encounters between particles and planets. The radiation pressure and drag forces were inserted into the Keplerian and kick parts of the integrator, respectively. The change to the Keplerian part was trivially done by substituting $m_\odot$ by $m_\odot(1 - \beta)$, where β is given by Equation (3).

The code tracks the orbital evolution of a particle that revolves around the Sun and is subject to the gravitational perturbations of seven planets (Venus to Neptune) until the particle impacts a planet, is ejected from the solar system, or drifts to within 0.03 AU from the Sun. We removed particles that evolved to $R < 0.03$ AU because the orbital period for $R \lesssim 0.03$ AU is not

properly resolved by our integration time step. In Section 4.2, we also consider the effect of collisional disruption by removing particles from the simulations when they reach their assumed physical lifespan. We followed 1000–5000 particles for each D, source, and parameter value(s) that define that source.

3.3. Thermal Emission of Particles

Particles were assumed to be isothermal, rapidly rotating spheres. The absorption was assumed to occur into an effective cross section πs^2, and emission out of $4\pi s^2$. The infrared flux density (per wavelength interval $d\lambda$) per unit surface area at distance r from a thermally radiating particle with radius s is

$$F(\lambda) = \epsilon(\lambda, s) B(\lambda, T) \frac{s^2}{r^2}, \quad (4)$$

where ϵ is the emissivity and $B(\lambda, T)$ is the energy flux at $(\lambda, \lambda + d\lambda)$ per surface area from a blackbody at temperature T:

$$B(\lambda, T) = \frac{2\pi hc^2}{\lambda^5} \left[e^{hc/\lambda kT} - 1 \right]^{-1}. \quad (5)$$

In this equation, $h = 6.6262 \times 10^{-34}$ J s is the Planck constant, $c = 2.99792458 \times 10^8$ m s^{-1} is the speed of light, and $k = 1.3807 \times 10^{-23}$ J K^{-1} is the Boltzmann constant. We used $\epsilon = 1$ which should be roughly appropriate for the large particles used in this work. See NVBS06 for a more precise treatment of $\epsilon(\lambda, s)$ for dust grains composed of different materials.

To determine the temperature of a particle at distance R from the Sun, we used the temperature variations with R that were proposed by different authors from spectral observations of the zodiacal cloud (e.g., Dumont & Levasseur-Regourd 1988; Renard et al. 1995; Leinert et al. 2002; Reach et al. 2003). For example, Leinert et al. (2002) proposed that $T(R) = 280/R^{0.36}$ K near $R = 1$ AU from ISOPHOT spectra. We used $T(R) = T_{1\mathrm{AU}}/R^{\delta}$ K, where $T_{1\mathrm{AU}}$ is the temperature at 1 AU and δ is a power index. We varied $T_{1\mathrm{AU}}$ and δ to see how our results depend on these parameters. Values of $T_{1\mathrm{AU}} \approx 280$ K and $\delta = 0.5$ correspond to the equilibrium temperature of large dark particles. Values $\delta < 0.5$ would be expected, for example, for fluffy particles with small packing factors (e.g., Gustafson et al. 2001). Note that the power law is used here as a simple empirical parameterization of the temperature gradient. The real temperature gradient is likely to be a more complicated function of the heliocentric distance (and particle properties).

3.4. Synthetic Observations

To compare our results with *IRAS* observations described in Section 2, we developed a code that models thermal emission from distributions of orbitally evolving particles and produces infrared fluxes that a space-borne telescope would detect depending on its location, pointing direction, and wavelength. See NVBS06 for a detailed description of the code.

In brief, we define the brightness integral along the line of sight of an infrared telescope (defined by fixed longitude l and latitude b of the pointing direction) as

$$\int_{a,e,i} da\,de\,di \int_0^{\infty} dr\, r^2 \int_D dD\, F(D, r) N(D; a, e, i) S(R, L, B), \quad (6)$$

where r is the distance from the telescope and $F(D,r)$ is the infrared flux (integrated over the wavelength range of the telescope's system) per unit surface area at distance r from a thermally radiating particle with diameter D. $S(R, L, B)$ defines the spatial density of particles as a function of the heliocentric distance, R, longitude, L, and latitude, B (all functions of r as determined by geometry from the location and pointing direction of the telescope). $N(D; a, e, i)$ is the number of particles having effective diameter D and orbits with semimajor axis, a, eccentricity, e, and inclination, i.

We evaluate the integral in Equation (6) by numerical renormalization (see NVBS06). $F(D,r)$ is calculated as described in Section 3.3. $N(D; a, e, i)$ is obtained from numerical simulations in Section 3.2. $S(R, L, B)$ uses theoretical expressions for the spatial distribution of particles with fixed a, e, and i, and randomized orbital longitudes (Kessler 1981; NVBS06).

We assume that the telescope is located at $(x_t = r_t \cos\phi_t,\ y_t = r_t \sin\phi_t,\ z_t = 0)$ in the Sun-centered reference frame with $r_t = 1$ AU. Its viewing direction is defined by a unit vector with components (x_v, y_v, z_v). In Equation (6), the pointing vector can be also conveniently defined by longitude l and latitude b of the pointing direction, where $x_v = \cos b \cos l$, $y_v = \cos b \sin l$, and $z_v = \sin b$. As described in Section 2, we fix the solar elongation $l_\odot = 90^\circ$ and calculate the thermal flux of various particle populations as a function of b and wavelength. The model brightness profiles at 12, 25, and 60 μm are then compared with the mean *IRAS* profiles shown in Figure 2.

To check our code, known as Synthetic InfraRed Telescope (SIRT), we programmed a particle version of the algorithm, which should be in many ways similar to the core algorithm in SIMUL (Dermott et al. 1988; see also Dermott et al. 2001). The particle version inputs the orbital elements of particles obtained in the orbital simulations (Section 3.2) and produces their orbit clones that are uniformly spread over 2π in mean anomaly M. Thus, every test particle is assumed to trace a cloud of real particles having the same orbit as the test particle but different angular locations along the orbit. See Vokrouhlický et al. (2008; their Section 2.5) for a technical description of the algorithm. This procedure is based on the assumption that any concentration of particles with a specific M value would be quickly dispersed by the Keplerian shear. We employ this procedure to improve the resolution. Without it, the number of integrated test particles would be too small to obtain a useful result.

To be able to compare the results of the particle algorithm with SIRT, the particle algorithm must also use smooth distributions in perihelion longitude ϖ and nodal longitude Ω. This is achieved by generating additional orbital clones with ϖ and Ω uniformly spread over 2π. Figure 4 shows examples of the results obtained from the particle algorithm and SIRT. The agreement between the two codes is excellent which gives us confidence that both codes work properly. We find that the SIRT algorithm based on the Kessler distribution is much faster than the particle one. For this reason, we use the original SIRT code in this study.

4. RESULTS

Our primary model parameters are the relative contribution of different sources to the zodiacal cloud. The total model flux as a function of the ecliptic latitude is obtained as

$$F_{\mathrm{model}}(b) = \alpha_{\mathrm{AST}} F_{\mathrm{AST}} + \alpha_{\mathrm{JFC}} F_{\mathrm{JFC}} + \alpha_{\mathrm{HTC}} F_{\mathrm{HTC}} + \alpha_{\mathrm{OCC}} F_{\mathrm{OCC}}, \quad (7)$$

where α are coefficients that satisfy $\alpha_{\mathrm{AST}} + \alpha_{\mathrm{JFC}} + \alpha_{\mathrm{HTC}} + \alpha_{\mathrm{OCC}} = 1$, and F_{AST}, F_{JFC}, F_{HTC}, and F_{OCC} are model fluxes obtained for different sources. We normalize them so that the ecliptic model

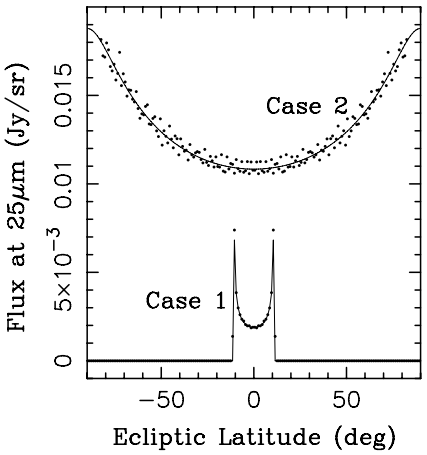

Figure 4. Comparison between results obtained from the particle algorithm (dots) and SIRT (solid lines). Case 1 corresponds to asteroidal particles with $a = 2.5$ AU, $e = 0.1$, and $i = 10°$. Case 2 corresponds to cometary particles crossing Earth's orbit with $a = 1$ AU, $e = 0.5$, and $i = 50°$. In both cases, we assumed that particles have $D = 100$ μm and are distributed randomly in Ω, ϖ, and M. The flux at 25 μm was normalized to a population of 10^{15} particles in Case 1 and 2×10^{15} particles in Case 2. Observations with $r_t = 1$ AU and $l_\odot = 90°$ were assumed. In Case 2, the particle algorithm shows a scatter around the exact solution due to the rough resolution of the distribution near the telescope's location. We used 5×10^{10} orbit clones in the particle algorithm.

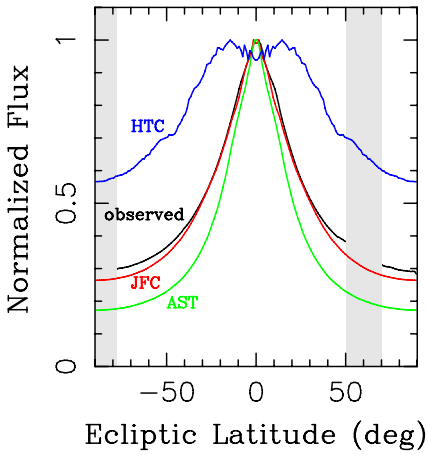

Figure 5. Comparison of the 25 μm profiles produced by different sources with *IRAS* observations. The black line shows our mean *IRAS* scan for $l_\odot = 90°$. The colored lines show profiles expected from different source populations: asteroids (green), JFCs (red), and HTCs (blue). The OCC flux, not shown here for clarity, is a nearly constant function of latitude. The maximum flux in each profile has been normalized to 1. We used $D = 100$ μm and $t_{JFC} = 12{,}000$ yr. The main differences between profiles are not sensitive to the exact choice of D and other model parameters.

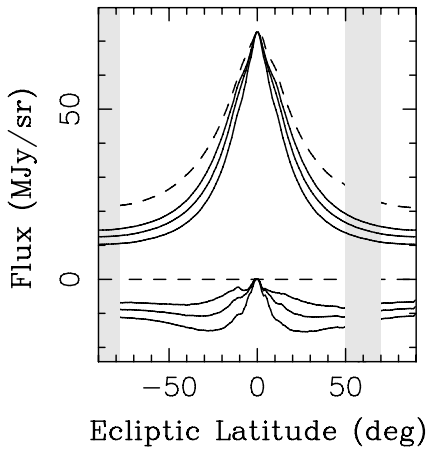

Figure 6. Dependence of the shape of 25 μm profiles produced by asteroidal particles on D. The dashed line shows the mean 25 μm *IRAS* profile for $l_\odot = 90°$. The upper solid curves show the model results for the same wavelength and elongation. The bottom lines show the residual flux obtained by subtracting the model flux from the mean *IRAS* profile. Results for $D = 30$, 100, and 300 μm asteroidal particles are shown with slightly broader profiles corresponding to larger D. The profiles for $D = 10$ and 1000 μm, not shown here, are narrower than the ones for $D = 30$ μm. For $D = 1000$ μm, this is mainly due to the effects of disruptive collisions that destroy large grains before they could evolve down to 1 AU (see discussion in Section 4.2). None of the model profiles obtained with asteroidal particles can match *IRAS* observations.

flux from each source is equal to that of the mean observed flux at $b = 0$. Coefficients α therefore give the relative contribution of different sources at the ecliptic.

The model flux profiles depend on the particle size, wavelength, and for JFCs also on the assumed value of t_{JFC}. As described in Section 3.2, we tracked particles with $10 < D < 1000$ μm. These different sizes are treated individually in Equation (7). In particular, we do not attempt to construct plausible size–frequency distributions for different sources. It is therefore assumed that a single characteristic particle size, or a narrow range of sizes, can be effectively used to model the observed MIR flux. This assumption needs to be verified later.

In Section 4.1, we first consider a model where the lifespan of particles is limited by their dynamical lifetime. Effects of particle disruptions are discussed in Section 4.2.

4.1. Collision-free Model

Figure 5 shows the 25 μm flux of $D = 100$ μm particles produced by different source populations. Note that these profiles do not sensitively depend on the particle size (see Figures 6 and 7 for the results for different D). Instead, the main differences between results for different source populations in Figure 5 reflect the initial orbit distribution of particles in each source and their orbit evolution. Therefore, these profiles can help us to identify the source population(s) that can best explain *IRAS* observations.

The asteroidal particles produce a profile with a very sharp peak centered at the ecliptic. The emission from asteroidal particles near the ecliptic poles is relatively faint. The polar emission comes from the particles that evolved by PR drag from $a > 2$ AU to $R = 1$ AU. While most asteroidal particles indeed reach 1 AU, they pass too briefly near $b = \pm 90°$ to produce important polar fluxes. This is why most radiation is received from $b \sim 0$, where the telescope collects the thermal emission of particles over a wide distance range. A broader distribution of orbital inclinations is apparently needed to match *IRAS* measurements.

The profile produced by HTC particles is much broader than the observed one (Figure 5). In this case, the magnitude of the polar fluxes is ≈1/2 of that near the ecliptic. This result reflects the very broad inclination distribution of HTCs (Section 3.1). A potentially significant contribution of HTCs to the zodiacal cloud is also problematic because the two large HTCs, 109P/Swift-Tuttle and 1P/Halley, tend to librate about mean-motion resonances, causing relatively stable orbits for long periods of time. Thus, dust released by HTCs is expected to be concentrated along certain locations on the sky making it difficult to explain the smooth profile of the zodiacal dust. Note also that Altobelli et al. (2007) have not detected HTC particle impacts in the Cassini dust experiment, indicating that HTC particles are relatively sparse.

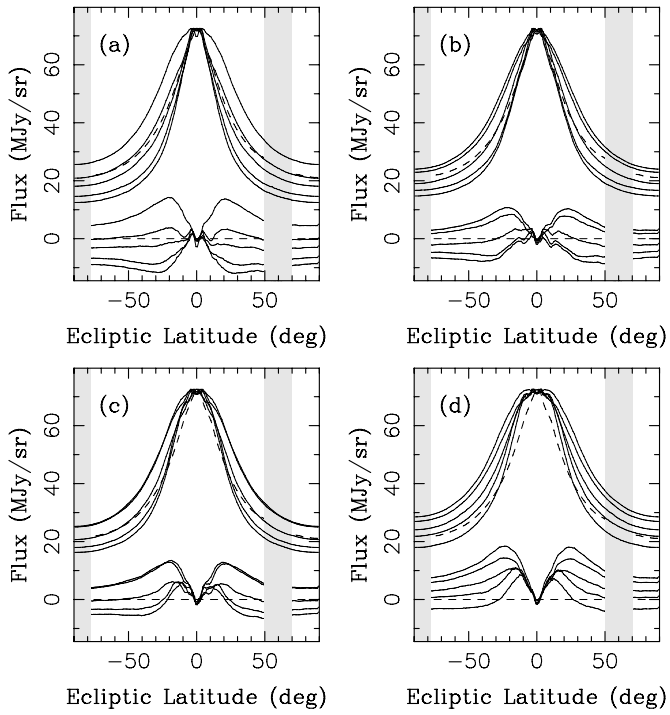

Figure 7. Dependence of the shape of 25 μm profiles produced by JFC particles on D and $t_{\rm JFC}$. The panels show results for different $t_{\rm JFC}$: (a) $t_{\rm JFC}$ = 12,000 yr, (b) $t_{\rm JFC}$ = 30,000 yr, (c) $t_{\rm JFC}$ = 50,000 yr, and (d) $t_{\rm JFC}$ = 100,000 yr. The dashed line in each panel shows the mean 25 μm *IRAS* profile for $l_\odot = 90^\circ$. The upper solid curves show the model results for the same elongation. The bottom lines show the residual flux obtained by subtracting the model fluxes from the mean *IRAS* profile. Results for D = 10, 30, 100, 300, and 1000 μm are shown in each panel with broader profiles corresponding to larger D. Some of these model profiles do not match *IRAS* observations well. Specifically, $t_{\rm JFC} > 50{,}000$ yr, $D > 300$ μm, and $D = 10$ μm can be clearly ruled out.

The OCC particles, which have a nearly isotropic inclination distribution, produce the MIR flux that is constant in latitude (not shown in Figure 5). Therefore, the ecliptic and polar fluxes from OCC particles are roughly the same and do not match observations. We conclude that a single-source model with either asteroidal, HTC, or OCC particles cannot match the observed profile of the zodiacal cloud.

We are left with JFCs. It is notable that the width and shape of the JFC profile in Figure 5 closely match observations. The only slight difference is apparent for large ecliptic latitudes where the model flux, shown here for $D = 100$ μm and $t_{\rm JFC}$ = 12,000 yr, is slightly weaker than the one measured by *IRAS*. We will discuss this small difference below and show that it could be explained if: (1) slightly smaller JFC particles were used, and/or (2) the zodiacal cloud has a faint isotropic component. We thus believe that the close resemblance of our model JFC profile with *IRAS* data is a strong indication that *JFCs are the dominant source of particles in the zodiacal cloud.*

Since asteroids and active JFCs have similar inclination distributions (Hahn et al. 2002), it may seem surprising that JFC particles produce substantially wider MIR flux profiles than asteroidal particles. By analyzing the results of our numerical integrations, we find that the encounters with terrestrial planets and secular resonances are apparently not powerful enough to significantly affect the inclination distribution of drifting asteroidal particles. The inclination distributions of the asteroidal particles and their source main belt asteroids are therefore essentially the same ($\approx 10^\circ$ mean i). On the other hand, we find that JFC particles are scattered by Jupiter before they are able to orbitally decouple from the planet and drift down to 1 AU. This results in a situation where the inclination distribution of JFC particles is significantly broader ($\approx 20^\circ$ mean i for $R < 3$ AU) than that of their source JFCs. This explains Figure 5 and shows limitations of the arguments about the zodiacal cloud origin based on the comparative analysis of sources (e.g., Hahn et al. 2002).

We will now address the question of how the MIR fluxes from the JFC particles depend on D and $t_{\rm JFC}$. We define

$$\eta^2 = \frac{1}{\pi}\int_{-\pi/2}^{\pi/2} \frac{[F_{\rm IRAS}(b) - F_{\rm model}(b)]^2}{\sigma^2(b)}\, db, \qquad (8)$$

where $F_{\rm IRAS}$ is the mean *IRAS* flux, σ is the standard deviation of $F_{\rm IRAS}$ determined from the spread of representative *IRAS* scans for each b (Section 2), and $F_{\rm model} = F_{\rm JFC}$ (i.e., $\alpha_{\rm JFC} = 1$ and $\alpha_{\rm AST} = \alpha_{\rm HTC} = \alpha_{\rm OCC} = 0$ in Equation (7)). Note that the integration in Equation (8) is set to avoid the intervals in b with strong galactic emission.

While the definition of η^2 in Equation (8) is similar to the usual χ^2 statistic (e.g., Press et al. 1992), we will not assign a rigorous probabilistic meaning to the η^2 values obtained from Equation (8). This is mainly because it is not clear whether the σ values computed in Section 2 from the *IRAS* data can adequately represent the measurement errors. Instead, we will use Equation (8) only as an indication of whether a particular model is more reasonable than another one. Models with $\eta^2 \lesssim 1$ will be given priority. For a reference, the JFC model in Figure 5 gives $\eta^2 = 5.1$.

We calculated η^2 as a function of D and $t_{\rm JFC}$ to determine which values of these parameters fit *IRAS* observations best. We found that the best fits with $\eta^2 < 10$ occur for $30 \leqslant D \leqslant 100$ μm and $t_{\rm JFC} \leqslant 30{,}000$ yr.

Figure 7 illustrates how the shape of the 25 μm profile produced by JFC particles depends on D and $t_{\rm JFC}$. The profiles become wider with increasing D and $t_{\rm JFC}$ values. For $t_{\rm JFC}$ = 12,000 yr, the best results were obtained with $D = 30$ μm and $D = 100$ μm ($\eta^2 = 3.2$ and 5.1, respectively). The profiles for $D = 10$ μm are too narrow and clearly do not fit data well ($\eta^2 = 70$), while those for $D = 1000$ μm are slightly too wide ($\eta^2 = 58$). We also found that there are no really good fits with $t_{\rm JFC} > 30{,}000$ yr, because the profiles are too broad near the ecliptic independently of the particle size.

The best single-source fits discussed above have $\eta^2 > 1$ which is not ideal. According to our additional tests this is probably not due to the coarse resolution and studied range of D and $t_{\rm JFC}$. Instead, this may point to (1) a subtle problem with our JFC model, and/or (2) the possibility that additional minor sources (such as asteroids, OCCs, or HTCs) should be included in the model. Option (1) is difficult to test unless a better model of the JFC population becomes available. Here, we concentrate on (2) because an ample evidence exists (e.g., for $\sim$10% near-ecliptic asteroid contribution from asteroid dust band modeling) that these additional sources may be relatively important.

We start by discussing the results obtained by assuming that the zodiacal cloud has two sources. The motivation for considering the two-source model was the following. First, we wanted see whether a combination of two sources could successfully fit the observed profile. Second, we attempted to place upper limits on the contributions of asteroid, OCC, and HTC sources. While it is obvious that models with more than two sources can be tuned to fit the data better, it is not clear whether more than two sources are actually required. Our two-source models were used to test these issues.

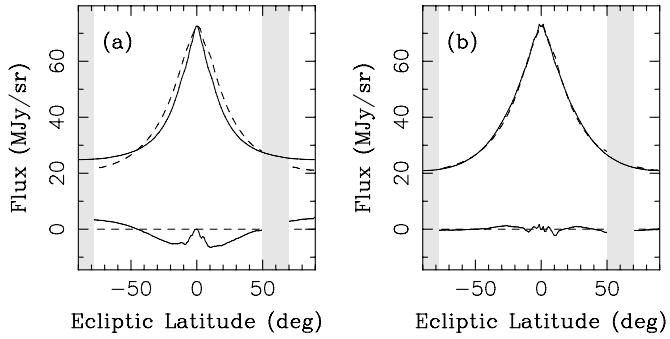

Figure 8. Examples of fits where we modeled the zodiacal cloud as having two sources. Fluxes at 25 μm are shown. (a) The best-fit model with asteroid and OCC sources. This model does not fit *IRAS* observations well. The model profile is too narrow near the ecliptic and too wide overall. (b) Our best two-source model. Here, we used $\alpha_{\rm JFC} = 0.97$, $\alpha_{\rm OCC} = 0.03$, $D = 100$ μm, and $t_{\rm JFC} = 12,000$ yr. The faint isotropic component improves the fit quality so that $\eta^2 = 0.36$ in (b). This may suggest that the zodiacal cloud contains a small but significant fraction of OCC particles.

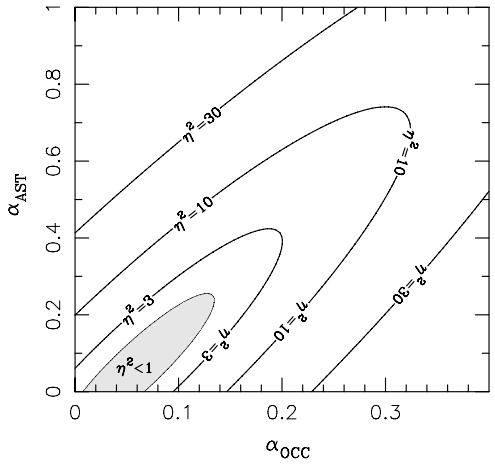

Figure 9. Model constraints on the contribution of asteroid and OCC particles to the zodiacal cloud. Here, we used a three-source model with $D = 100\,\mu$m and $\alpha_{\rm HTC} = 0$. For a range of the $\alpha_{\rm OCC}$ and $\alpha_{\rm AST}$ values, we set $\alpha_{\rm JFC} = 1-\alpha_{\rm OCC}-\alpha_{\rm AST}$, and calculated η^2 (Equation (8)) for each model. The contours show $\eta^2 = 3$, 10, and 30. The shaded area denotes the parameters of our best-fit models with $\eta^2 < 1$. These models have $\alpha_{\rm OCC} < 0.13$ and $\alpha_{\rm AST} < 0.22$ thus placing an upper limit on the near-ecliptic contribution of asteroid and OCC particles.

In the first test, we used the two-source model with asteroids and OCCs (i.e., $\alpha_{\rm JFC} = \alpha_{\rm HTC} = 0$ in Equation (7)). We found that this particular model produces unsatisfactory fits ($\eta^2 > 10$) to *IRAS* observations for all particle sizes considered here (10–1000 μm) (Figure 8(a)). The model profile is significantly narrower near the ecliptic, where the asteroid component prevails, and is too wide for $|b| \gtrsim 40^\circ$, where the OCC component prevails. This happens mainly due to the fact that the asteroid dust is confined to the ecliptic plane and produces a very narrow profile near the ecliptic (Figure 5). We also find it unlikely that two so distinct populations of objects, such as the main belt asteroids and OCCs, would have comparable dust production rates. Thus, we believe that the two-source model with asteroid and OCC dust can be dismissed.

In the second test, we set $\alpha_{\rm OCC} = \alpha_{\rm HTC} = 0$ and considered models of the zodiacal cloud with the JFC and asteroid components. We found that a small contribution of asteroid dust can improve the fits. For example, $\eta^2 = 0.92$ for the $D = 30$ μm JFC particles with $\alpha_{\rm JFC} = 0.9$ and $t_{\rm JFC} = 12{,}000$ yr, and $D = 100\,\mu$m asteroidal particles with $\alpha_{\rm AST} = 0.1$. This represents a significant improvement from $\eta^2 = 3.2$ that we obtained for a single-source model with JFC particles only. Values $\alpha_{\rm AST} \gtrsim 0.3$ are clearly unsatisfactory because $\eta^2 > 10$ for $\alpha_{\rm AST} > 0.3$. Also, $\eta^2 > 3.1$ for $\alpha_{\rm AST} > 0.2$ which shows that the fit does not improve when we add a $\gtrsim$20% asteroid contribution. These results suggest that a very large asteroid contribution to the zodiacal cloud can be ruled out. This agrees with the conclusions of NVBS06 who found that $\alpha_{\rm AST} \lesssim 0.15$ from modeling of the main asteroid dust bands.

Finally, the two-component model with the JFC and isotropic OCC sources can fit the data very well (Figure 8(b)). With $D = 100\,\mu$m and $t_{\rm JFC} = 12{,}000$ yr, corresponding to one of our best single-source fits with JFCs, $\alpha_{\rm JFC} = 0.97$ and $\alpha_{\rm OCC} = 0.03$, we find that $\eta^2 = 0.36$, by far the best fit obtained with any two-source model. As Figure 8(b) shows, the fit is excellent. We may thus find an evidence for a small contribution of OCC particles to the zodiacal cloud. A much larger OCC contribution is not supported by the data because the fit gets significantly worse for $\alpha_{\rm OCC} > 0.1$. For example, $\eta^2 > 10$ for $\alpha_{\rm OCC} > 0.15$ which is clearly unsatisfactory. A large contribution of OCC particles can therefore be rejected.

We propose based on the results described above that the zodiacal cloud has a large JFC component ($\alpha_{\rm JFC} \gtrsim 0.9$), and small asteroid/OCC components ($\alpha_{\rm AST} \lesssim 0.2$ and $\alpha_{\rm OCC} \lesssim 0.1$). To verify this conclusion, we considered three-component models with $\alpha_{\rm HTC} = 0$ and used $\alpha_{\rm JFC}$, $\alpha_{\rm AST}$, and $\alpha_{\rm OCC}$ as free parameters. We found that the best two-source fit with $\alpha_{\rm JFC} = 0.97$ and $\alpha_{\rm OCC} = 0.03$ cannot be significantly improved by including a small asteroid contribution. Similarly, the fit with $\alpha_{\rm JFC} = 0.9$ and $\alpha_{\rm AST} = 0.1$ cannot be improved by adding a small OCC contribution. Thus, the asteroid/OCC contributions cannot be constrained independently because their effects on the combined profiles can be compensated by adjusting the D and $t_{\rm JFC}$ values of the dominant JFC particles.

If we set the parameters of the dominant JFC particles to be $D = 100$ μm and $t_{\rm JFC} = 12{,}000$ yr, however, the $\alpha_{\rm AST}$ and $\alpha_{\rm OCC}$ values can be constrained much better (Figure 9). For example, models with $\eta^2 < 1$ require that $\alpha_{\rm AST} < 0.22$ and $\alpha_{\rm OCC} < 0.13$. Thus, under reasonable assumptions, the contribution of asteroid particles to the near-ecliptic *IRAS* fluxes is probably < 10%–20%, in agreement with the results obtained in NVBS06 from modeling of the asteroid dust bands. This means that asteroid dust contributes only by <10% to the overall zodiacal dust emission at MIR wavelengths. The thermal emission of OCC particles can constitute as much as ∼10% of the near-ecliptic emission with ≈5% providing the best fits (Figure 9). When integrated over latitude, the overall OCC component in the zodiacal cloud is likely to be $\lesssim$10%.[6]

For the sake of consistency with the results suggested from modeling of the asteroid dust bands (see Section 3.1; NVBS06), we impose a small asteroid contribution in the JFC/OCC model. Figure 10 shows our preferred fit at different *IRAS* wavelengths. The η^2 values of this fit in different wavelengths are the following: 0.29 at 12 μm, 0.35 at 25 μm, and 0.06 at 60 μm. This is very satisfactory. Since our model does not include detailed emissivity properties of dust grains at different wavelengths

[6] Note that we are unable to distinguish in the model between the uncertainty in instrumental isotropic brightness of *IRAS* measurements and the OCC contribution. We also do not know how much of the brightness of the faintest part of the sky is cosmological (or galactic). For these reasons, the OCC contribution to the zodiacal cloud is difficult to calibrate from *IRAS* observations alone.

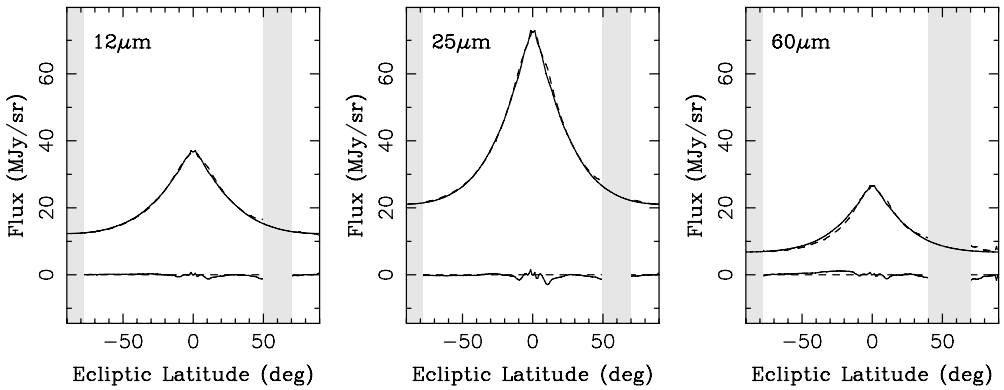

Figure 10. Our preferred fit with $\alpha_{\rm JFC} = 0.85$, $\alpha_{\rm OCC} = 0.05$, $\alpha_{\rm AST} = 0.1$, and $\alpha_{\rm HTC} = 0$. Particles with $D = 100$ μm and $t_{\rm JFC} = 12{,}000$ yr were used here. The dashed lines show the mean *IRAS* profiles at 12, 25, and 60 μm. The upper and lower solid lines are the model and residual profiles, respectively. The wiggle in the residual profiles for $|b| < 10^\circ$ may occur due to a slight problem with our asteroid dust band model.

(Section 3.3), we set the emissivity at 25 μm to be 1 and fit for the emissivities at 12 and 60 μm. We found that the relative emissivities at 12 and 60 μm that match the data best are 0.76 and 0.87, respectively. Such a variability of MIR emissivity values at different wavelengths is expected for $D \approx 100$ μm silicate particles with some carbon content (NVBS06). Note also that our preferred D values ($D \approx 100$ μm) are within the range of dominant sizes of particles at 1 AU as determined from spacecraft impact experiments ($D = 20$–200 μm; Grün et al. 1985).

4.2. Effect of Disruptive Collisions

The observational evidence for collisional disruption of interplanetary particles is undeniable (see, e.g., Grün et al. 1985), yet it is very difficult to model the full collisional cascade in a computer code as each disrupted dust grain produces numerous fragments. The exponentially increasing number of particle fragments, which in reality exceeds 10^{25} for $D > 30$ μm (NVBS06), renders any full N-body integration impossible. To circumvent this problem, the N-body integration of a smaller number of "tracer" particles can be coupled with a Monte Carlo model for collisions as in NVBS06. This method is not ideal. Also, any model for the collisional cascade would suffer from our lack of detailed understanding of particle properties and their fragmentation during impacts.

Here, we opt for a very simple approximation of the effect of disruptive collisions. We assume that the collisional lifetime of particles is $t_{\rm col}(D)$ and stop the N-body integration of diameter D particles when $t = t_{\rm col}(D)$. Thus, particles keep the same D for $t < t_{\rm col}(D)$ and vanish at $t = t_{\rm col}(D)$. This is a very crude approximation of the real collisional cascade, in which particles can be eroded by small collisions and do not vanish upon disruptive impacts (but produce a range of new particle sizes). Also, $t_{\rm col}(D)$ should be a function of R while we assume here that it is not. Still, as we show below, our simple model should be able to capture the main effects of particle collisions.

Our choice of $t_{\rm col}(D)$ is motivated by the published estimates of the collisional lifetime of particles based on satellite impact rates and meteor observations. For example, Grün et al. (1985) argued that the collisional lifetime of $D = 1$ mm particles at 2.5 AU should be $\sim 10^4$ yr (see also Jacchia & Whipple 1961). This relatively short lifetime is a consequence of the dominant population of $D \approx 100$–300 μm particles in the inner solar system (e.g., Love & Brownlee 1993) that are capable of disrupting mm-sized particles upon impacts.

For comparison, the approximate PR drag timescale of particles to spiral down from 2.5 AU to 1 AU is $t_{\rm PR} = 2500$ yr $\times \rho s$, which for $\rho = 2$ g cm^{-3} and $s = 500$ μm gives $t_{\rm PR} = 2.5 \times 10^6$ yr. Thus, the PR drag lifetime of these large particles is significantly longer than $t_{\rm col}$, indicating that they must disrupt before they can significantly evolve by PR drag. Using this assumption in the model, we found that the profiles produced by large JFC particles with $t_{\rm col} \sim 10^4$ yr are much narrower in latitude than the ones we obtained in Section 4.1. This is because large particles die before they can evolve to $R \sim 1$ AU, where they could contribute to polar fluxes. The zodiacal cloud cross section therefore cannot be dominated by large JFC grains. The large grains are important to explain radar and optical observations of meteors (see Section 5.3; Taylor & Elford 1998; Jenniskens 2006; Wiegert et al. 2009).

On the other side of the size spectrum, $D < 10$ μm particles have $t_{\rm PR} \ll t_{\rm col}$ due to the lack of small $D < 1$ μm impactor particles that are blown out of the solar system by radiation pressure, and because the PR drag timescale is short for small D (see, e.g., Dermott et al. 2001). Thus, the small particles are expected to spiral down by PR drag from their initial orbits to $R < 1$ AU without being disrupted. Our original results described in Section 4.1 are therefore correct for small particles. We showed in Section 4.1 that $D < 30$ μm JFC particles do not fit *IRAS* observations well.

Since $t_{\rm PR} \ll t_{\rm col}$ for small particles and $t_{\rm PR} \gg t_{\rm col}$ for large ones, there must exist an intermediate particle size for which $t_{\rm PR} \sim t_{\rm col}$. These intermediate-size particles are expected to be very abundant in the zodiacal cloud simply because they have the longest lifetimes. Grün et al. (1985) and others argued that the transition from the PR drag to collision-dominated regimes must happen near 100 μm. This is consistent with the LDEF measurements which imply that the $D \approx 200$ μm particles represent the dominant mass fraction at $R = 1$ AU (Love & Brownlee 1993).

The question is therefore how to model collisional effects for $D \sim 100$ μm. This is not a simple problem because the effects of the full collisional cascade, including gradual erosion of particles and their supply from breakups of the large ones, should be particularly important in this transition regime. It would be incorrect, for example, to take the Grün et al. estimates of $t_{\rm col}$ at their face value and remove particles when $t > t_{\rm col}$. In reality, each particle can accumulate PR drift during previous stages of evolution when it is still attached to its (slightly) larger precursor particles.

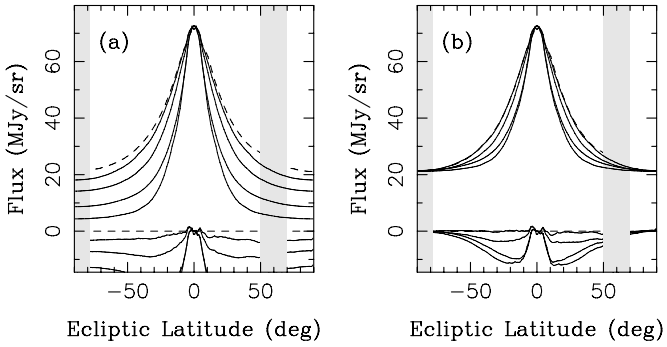

Figure 11. Dependence of the shape of 25 μm profiles produced by $D = 100$ μm JFC particles on t_{col}. The dashed line in each panel shows the mean 25 μm *IRAS* profile for $l_\odot = 90°$. The upper solid curves show the model results for the same elongation. The bottom lines show the residual flux obtained by subtracting model fluxes from the mean *IRAS* profile. Results for $t_{col} = 10^4$, 10^5, 5×10^5, and 10^6 yr are shown in each panel with broader profiles corresponding to the larger t_{col} values. In panel (a), we show results for the single-source model with JFC particles only. The results of the two-source model with JFC and OCC particles are illustrated in (b). We included the OCC component in the model to try to compensate for the deficient polar fluxes from JFC particles with short t_{col}. Profiles with $t_{col} \lesssim 5 \times 10^5$ yr do not match *IRAS* observations well.

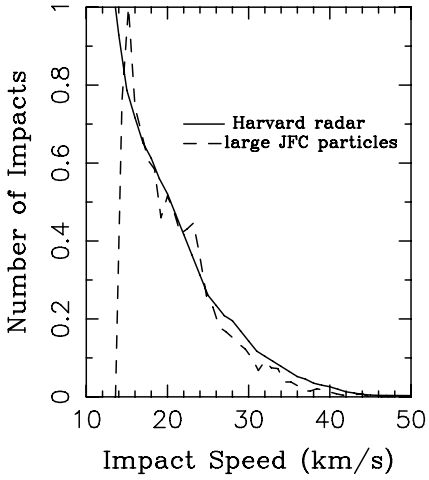

Figure 12. Comparison of atmospheric entry speeds of $D = 1$ mm JFC particles with $t_{col} = 10^4$ yr with the Harvard meteor radar data (Taylor 1995). There is a good agreement between the two distributions for >20 km s^{-1}. The number of impacts from large JFC particles drops at <15 km s^{-1}. The Harvard data are affected by strong biases for <20 km s^{-1}, because the detectable ionization level produced by a meteor is a strong function of meteor speed.

To test these issues, we assumed a wide range of effective t_{col} and calculated model JFC profiles for each of these cases. Figure 11 shows that the profiles obtained with $t_{col} \leqslant 5 \times 10^5$ yr are significantly narrower than the *IRAS* profiles, even if we tried to compensate for part of the apparent discrepancy by OCC particles (Figure 11(b)). On the other hand, profiles with $t_{col} \geqslant 6 \times 10^5$ yr are almost indistinguishable from the original results that we obtained in Section 4.1 with $t_{col} = \infty$. The transition between 5×10^5 yr and 6×10^5 yr occurs near the mean PR drag lifetime of $D = 100$ μm JFC particles in our model. It clearly makes a large difference whether particles are allowed to drift down to $R = 1$ AU or not. The main lesson we learn from this exercise is that *IRAS observations imply that the zodiacal cloud particles have been significantly affected by PR drag*.

4.3. Additional Constraints

Additional constraints on the micrometeoroid environment near 1 AU are provided by radar and optical observations of meteors. For example, Hunt et al. (2004) determined the meteor entry speeds from the high-gain ALTAIR radar. For 30 km s^{-1}, the minimum detectable mass is 10^{-6} g (corresponding to $D = 100$ μm for $\rho = 2$ g cm^{-3}), while only mm-sized and larger meteoroids can be detected by the ALTAIR radar for <20 km s^{-1}. The ALTAIR measurements represent a significant improvement in sensitivity relative to that of previous radar programs (e.g., Taylor 1995; Taylor & Elford 1998). For example, Taylor (1995) cited the minimum detectable mass of 10^{-4} g at 30 km s^{-1} for the Harvard meteor radar, corresponding to $D \gtrsim 500$ μm particles.

In Section 5.3, we estimate that the mean atmospheric entry speed of $D \sim 100$ μm zodiacal cloud particles is ≈14 km s^{-1}, and that >90% impact at <20 km s^{-1}. Thus, the ALTAIR and Harvard radars cannot detect the bulk of small zodiacal cloud particles impacting Earth at low speeds. These measurements are instead sensitive to large meteoroids, which carry relatively little total mass and cross section, have short t_{col}, and are expected to impact on JFC-like orbits. This explains why radar observation show little evidence for populations of small particles with orbits strongly affected by PR drag. In Figure 12, we compare the atmospheric entry speeds of $D = 1$ mm JFC particles with $t_{col} = 10^4$ yr with the Harvard radar data. This figure documents the dominant role of large JFC particles in meteor radar observations.

The spatial distribution of sporadic meteors shows several concentrations on the sky known as the helion/antihelion, north/south apex, and north/south toroidal sources (e.g., Younger et al. 2009, and the references therein). Wiegert et al. (2009) have developed a dynamical model to explain these observations. Their main result concerns the prominent helion/antihelion sources for which the large JFC particles clearly provide the best match. Our model for large JFC particles is in many ways similar to that of Wiegert et al. (2009). It should therefore be consistent with the observed relative strength of the helion/antihelion sources. The more recent high-gain antenna observations show that smaller meteoroids appear to show a weaker helion/antihelion source of eccentric short-period orbits (Mathews et al. 2001; Hunt et al. 2004; Galligan & Baggaley 2004). This implies that orbits of smaller particles should be more affected by PR drag (in agreement with Section 4.2).

The motion of interplanetary particles can be probed by high-resolution spectral observations of the zodiacal cloud. Reynolds et al. (2004) measured the profile of the scattered solar Mg I λ5184 Fraunhofer line in the zodiacal cloud. The measurements indicate a significant population of dust on eccentric and/or inclined orbits. In particular, the inferred inclination distribution is broad extending up to about 30°–40° with respect to the ecliptic plane. The absence of pronounced asymmetries in the shape of the profiles limits the retrograde population of particles to less than 10% of the prograde population.

These results are in a broad agreement with our model. As we discussed in Section 4.1, small JFC particles are scattered by Jupiter before they are able to orbitally decouple from the planet and drift down to 1 AU. This results in a situation where the inclination distribution of JFC particles is broad and extends beyond 20°. The model eccentricities of JFC particles show a broad range of values with most having $e = 0.1$–0.5 (see Section 5.3). This is in a nice agreement with the analysis of Ipatov et al. (2008) who found that $e \sim 0.3$ best fits the Reynolds et al. data.

5. IMPLICATIONS

Given the results described in Section 4 we are now in the position to estimate the total cross section and mass of particles in the zodiacal cloud, the current and historical accretion rates of dust by planets and the Moon, and discuss the implications of our work for studies of MMs and debris disks. We address these issues below.

5.1. Zodiacal Cloud Mass

According to our preferred model with the dominant contribution of JFC particles to the zodiacal cloud, the inner circumsolar dust complex has the total cross section area of $(2.0 \pm 0.5) \times 10^{11}$ km^2. This is a factor of $\sim$10 larger than the cross section of asteroidal particles in the main asteroid dust bands (NVBS06). The uncertainty of the total cross section was estimated from the range of values obtained for models with $\eta^2 < 3$. Also about 40% of the total estimated cross section of the zodiacal cloud, or $\approx 8 \times 10^{10}$ km^2, is in particles that reside inside Jupiter's orbit (i.e., with $R < 5$ AU).

The estimated values are comparable to the effective emitting area of the zodiacal cloud defined as 1 ZODY in Gaidos (1999) (1 ZODY $= 1.7 \times 10^{11}$ km^2, assuming blackbody emission at 260 K and a bolometric luminosity of $8 \times 10^{-8}\ L_\odot$, where $L_\odot$ is the Sun's value; Reach et al. 1996; Good et al. 1986). Note, however, that we estimate in Section 5.5 that the bolometric luminosity of the inner zodiacal cloud is $\sim$2.5 times larger than the one assumed by Gaidos (1999).

The total mass of the zodiacal cloud is a function of the unknown particle density and loosely constrained dominant particle size. With $\rho = 2$ g cm^{-3} and $D = 200\ \mu$m, we estimate that the total mass is $m_{\rm ZODY} = 5.2 \times 10^{19}$ g, which is roughly equivalent to that of a 37 km diameter body. The zodiacal cloud therefore currently contains relatively little mass. Note that these estimates apply to the inner part of the circumsolar dust complex that is detectable at MIR wavelengths. The outer circumsolar dust complex beyond Jupiter is likely more massive due to the contribution from KB particles (e.g., Landgraf et al. 2002; Moro-Martín & Malhotra 2003). According to Greaves et al. (2004), the KB dust disk may represent up to $\sim 1.2 \times 10^{23}$ g. This is up to $\sim 3 \times 10^3$ times the mass of the inner zodiacal cloud estimated here. Note that this is an upper bound only and that the real KB dust disk can be much less massive.

Our mass estimate is at least a factor of $\sim$2 uncertain. For example, if $\rho = 1$ g cm^{-3} or $D = 100\ \mu$m, we find that $m_{\rm ZODY} = 2.6 \times 10^{19}$ g. These values are a factor of $\sim$2–4 lower than the mass of the zodiacal cloud suggested by NVBS06 from modeling of the asteroid dust bands. NVBS06 assumed that the radial distribution of zodiacal particles is similar to that of the asteroid dust bands, which is incorrect if JFCs are the dominant source. On the other hand, NVBS06 determined the realistic size distribution of zodiacal particles by tracking the collisional evolution, while we used the single-size distributions here.

We estimate that $\gtrsim$80% of the total mass at <5 AU should be contained in JFC particles. Since these particles can efficiently decouple from Jupiter by PR drag, a large fraction of the total mass is distributed relatively close to the Sun. (For reference, we find that 53%, 19%, and 3.7% of $D = 10$, 100, and 1000 μm particles released by JFCs, respectively, can decouple from Jupiter.) Figure 13 shows the mass fraction of JFC particles contained in a sphere of radius R around the Sun. The distribution is steep for $R < 5$ AU and shallower for $R > 5$ AU reflecting the orbital properties of our model JFC population.

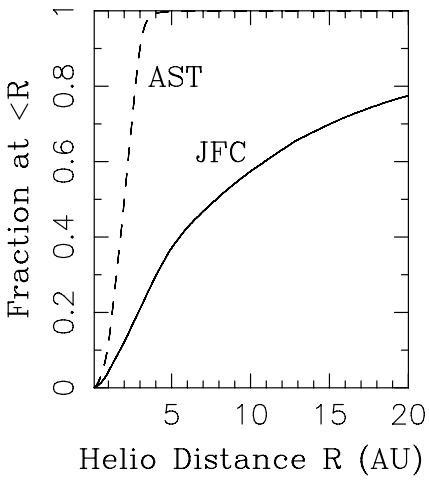

Figure 13. Cumulative distribution of JFC (solid line) and asteroidal (dashed) particles as a function of heliocentric distance R. For each R, the value on the Y-axis gives the fraction of particles (or equivalently fraction of the total mass) contained within a sphere of radius R around the Sun. The JFC particles show a shallower slope with about 70% having $R > 4$ AU. Conversely, 99% of asteroidal particles have $R < 4$ AU. Note that the distributions shown here have been normalized to 1 and do not reflect the actual relative contribution of JFC and asteroidal particles to the zodiacal cloud. This figure merely shows the trends in both populations with heliocentric distance.

About 30% of JFC particles, or about 1.6×10^{19} g in total mass (for $\rho = 2$ g cm^{-3} and $D = 200\ \mu$m), are located within $R < 4$ AU. Also, $\approx$10%, or about 5.2×10^{18} g, has $R < 2$ AU.

For a comparison, assuming that the asteroidal particles with $D = 200\ \mu$m and $\rho = 2$ g cm^{-3} contribute by 15% to the near-ecliptic MIR fluxes, we find that the total masses in asteroidal particles with $R < 2$ AU and $R < 4$ AU are 5.3×10^{17} g and 1.3×10^{18} g, respectively. Thus, the total mass (or number) ratio of JFC to asteroidal particles in the inner solar system is $\lesssim$10. Note that this estimate applies as far as the size distributions of JFC and asteroidal particles in the zodiacal cloud are similar, which is expected because both particle populations live in the common collisional environment and have similar PR drag timescales.

5.2. Mass Influx on Earth

We used the Öpik algorithm (Öpik 1951; Wetherill 1967) to estimate the terrestrial accretion rate of JFC particles expected from our model. For $30 < D < 300\ \mu$m, the average impact probability of JFC particles on the Earth is $\sim 5 \times 10^{-9}$ yr^{-1} per one particle in the zodiacal cloud. A similar value is obtained if the impact probability is estimated from the number of direct impacts recorded by the N-body integrator. Thus, in a steady state with $\sim 2 \times 10^{19}$ g in the zodiacal cloud, we estimate that $\sim 10^5$ tons of JFC particles should be accreted by the Earth annually. This is larger than the nominal Earth's accretion rate of 20,000–60,000 tons yr^{-1} as determined from LDEF (Love & Brownlee 1993) and the antarctic MM record (Taylor et al. 1996).

This may imply that the real Earth's accretion rate is somewhat larger than the LDEF values. Alternatively, the LDEF constraints may imply that the real mass of the zodiacal cloud is lower than the one estimated here. As we discussed above, the mass of the zodiacal cloud estimated here from the *IRAS* data is at least a factor of $\sim$2 uncertain. It is thus plausible that $m_{\rm ZODY} \sim 10^{19}$ g (e.g., if $\rho = 1$ g cm^{-3}), which would bring our results into a better agreement with LDEF. Additional

uncertainty in these estimates is related to the effects of collisional disruption of particles and continuous size distribution.

For comparison, if we assumed that $D = 200\ \mu$m asteroidal particles are producing the full near-ecliptic MIR flux measured by *IRAS*, the estimated terrestrial accretion rate of asteroidal particles would be 1.5×10^5 tons yr^{-1}. According to NVBS06 and the results obtained here, however, the asteroidal particles contribute by only ∼10% of the near-ecliptic MIR flux. Thus, we find that the asteroid particle accretion rate should be ∼15,000 tons yr^{-1}, or only ∼15% of the JFC particle accretion rate. The asteroidal particles should therefore represent a relatively minor fraction of IDPs and MMs in our collections. This explains the paucity of the ordinary chondritic material in the analyzed samples (see, e.g., Genge 2006).

Using the same assumptions, we estimate from our model that 16,000 tons yr^{-1} and 1600 tons yr^{-1} of JFC particles should be accreted by Mars and the Moon, respectively. The accretion rate of JFC particles on the Moon is thus only about ∼2% of Earth's accretion rate. This corresponds to a smaller physical cross section and smaller focusing factor of the Moon. The mass influx on Mars is ∼20% of Earth's accretion rate. For a comparison, 1600 tons and 100 tons of asteroidal particles are expected to fall on Mars and the Moon annually.

Love & Brownlee (1993) found from the LDEF impact record that $D \approx 200\ \mu$m particles should carry most of the mass of zodiacal particles near 1 AU, while we find here that $D \approx 100\ \mu$m provides the best fit to *IRAS* observations. This slight difference may be related to some of the limitations of our model. It can also be real, however, because the LDEF size distribution computed by Love & Brownlee (1993) is bending from the steep slope at $D > 300\ \mu$m to the shallow slope at $D < 50\ \mu$m. The cross section area should therefore be dominated by smaller particles than the mass. From Figure 4 in Love & Brownlee (1993), we estimate that $D \approx 100\ \mu$m particles should indeed dominate the total cross section area of the zodiacal cloud at 1 AU.

5.3. Cometary Origin of Micrometeorites

These results have implications for the origin of MMs. MMs are usually classified according to the extent of atmospheric heating they endure (e.g., Engrand & Maurette 1998). Cosmic spherules are fully melted objects. Scoriaceous MMs are unmelted but thermally metamorphosed objects. The fine-grained MMs and coarse-grained MMs are unmelted objects which can be distinguished on the basis of their grain size. Based on bulk composition, carbon content, and the composition of isolated olivine and pyroxene grains, fine-grained MMs and scoriaceous MMs, which appear to be thermally metamorphosed fine-grained MMs, are likely related to carbonaceous chondrites. It has been estimated that the ratio of carbonaceous to ordinary chondrite MMs is ∼6:1 or larger (see, e.g., Levison et al. 2009). This stands in stark contrast to the terrestrial meteorite collection, which is dominated by ordinary chondrites.

A possible solution to this discrepancy is that a large fraction of the collected MMs are particles from the JFCs. This possibility has to be seriously considered because we find here that the carbonaceous JFC grains should prevail, by a large factor, in the terrestrial accretion rate of micrometeoroids. It has been suggested in the past that a possible problem with this solution is that the cometary particles should encounter the Earth at large velocities (e.g., Flynn 1995), so that they either burn up in the atmosphere or are converted into cosmic spherules. Thus, while cometary particles could produce fully melted objects such as the cosmic spherules it was not clear whether the less thermally processed carbonaceous MMs, such as the fine-grained and scoriaceous MMs, may represent cometary material.

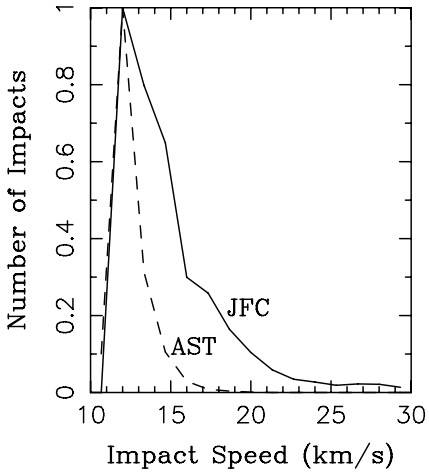

Figure 14. Model distributions of Earth-impact speed of JFC (solid line) and asteroidal (dashed) particles with $D = 200\ \mu$m. Since the effects of the gravitational focusing have been accounted for in the calculation, the minimum impact speed is equal to the escape velocity from Earth's surface, or about 11.2 km s^{-1}. The majority of JFC particles have impact speeds in the 11.2–15 km s^{-1} range. JFC particles with larger impact speeds have lower impact probability but are important for interpretation of the meteor radar data (e.g., Wiegert et al. 2009).

By assuming $t_{\rm col} \gtrsim 5 \times 10^5$ yr for $D = 100\ \mu$m as required by *IRAS* observations (see Section 4.2), we find from our model that the mean impact speed of $D \sim 200\ \mu$m JFC particles on Earth is ≈14.5 km s^{-1} (Figure 14; see Section 4.3 for a discussion of the size dependence of impact speed and its relevance to meteor observations). This value is only slightly higher than that of the asteroidal particles (≈12.5 km s^{-1}). The comparable impact speeds of JFC and asteroidal particles in our model are a consequence of PR drag which efficiently circularizes the orbits before they can reach 1 AU (Figure 15). We thus find that the impact speeds of the JFC particles are low and do not pose a serious problem. Based on this result and the high terrestrial accretion rate of JFC particles on Earth (Section 5.2), *we propose that the carbonaceous MMs in our collections are grains from the JFCs*. A large contribution from primitive material that may have been embedded into the main asteroid belt according to Levison et al. (2009) is probably not needed.

Dobrica et al. (2010) compared antarctic MMs with particles that were collected from JFC 81P/Wild (known also as Wild 2) by the Stardust spacecraft. They found that the bulk composition (CI-like) and petrography (presence of chondrules and calcium–aluminium-rich inclusions; CAIs) is similar. Moreover, MMs and 81P/Wild particles have strikingly similar mineralogy. For example, the pyroxene and olivine have similar abundances in both samples, which is unusual for most meteorite groups which typically have more olivine (Lauretta & McSween 2008). The same three types of sulfides (troilite, pyrrhotite, and pentlandite) were found both in MMs and Wild-2 particles. In addition, trace elements such as chromium and manganese have similar concentrations in the collected samples. Though phyllosilicates, present in some MMs (Engrand & Maurette 1998), were not found in Wild-2 particles, they were detected in JFC Tempel 1 (Lisse et al. 2006). Finally, Wild-2 particles and MMs have the same oxygen isotopic composition of chondrules and CAIs's components (Dobrica et al. 2010).

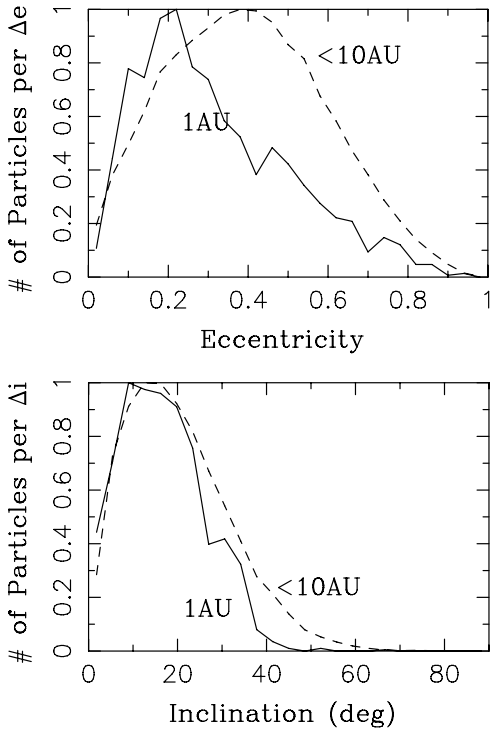

Figure 15. Eccentricity (top panel) and inclination (bottom) distributions of JFC particles in our model. The dashed lines show the distributions for all JFC particles with $R < 10$ AU. The solid lines show the distribution for $0.9 < R < 1.1$ AU. The upper plot illustrates that the orbits of JFC particles drifting by PR drag become nearly circularized before reaching 1 AU. The inclination distribution does not change much during this evolution.

These results indicate that MMs have physical properties similar to those of cometary particles, which is consistent with most MMs being derived from comets. This provides independent evidence (to that obtained from our dynamical model) for cometary origin of MMs.

5.4. Historical Brightness

It is believed that the main source of JFCs is the scattered trans-Neptunian disk, which should have decayed by a factor of ∼100 over the past ∼4 Gyr (LD97; Dones et al. 2004). If the JFC population decayed proportionally, we can estimate that the ecliptic component of the zodiacal dust should have been ∼100 times brighter initially that it is now. This corresponds to the near-ecliptic 25 μm flux of about 7×10^3 MJy sr^{-1}.

A different insight into the historical brightness of the zodiacal cloud can be obtained in the framework of the Nice model (Tsiganis et al. 2005), which is the most complete model currently available for the early evolution of the outer solar system. In the Nice model, the giant planets are assumed to have formed in a compact configuration (all were located at 5–18 AU). Slow migration was induced in these planets by gravitational interaction with planetesimals leaking out of a massive primordial trans-planetary disk. After a long period of time, most likely some 700 Myr after formation of the giant planets (Gomes et al. 2005), planets crossed a major mean-motion resonance. This event triggered a global instability that led to a violent reorganization of the outer solar system. Uranus and Neptune penetrated the trans-planetary disk, scattering its inhabitants throughout the solar system. Finally, the interaction between the ice giants and the planetesimals damped the orbits of these planets, leading them to evolve onto nearly circular orbits at their current locations.

The Nice model is compelling because it can explain many of the characteristics of the outer solar system (Tsiganis et al. 2005; Morbidelli et al. 2005; Nesvorný et al. 2007; Levison et al. 2008; Nesvorný & Vokrouhlický 2009). In addition, the Nice model can also provide an explanation for the Late Heavy Bombardment (LHB) of the Moon (Tera et al. 1974; Chapman et al. 2007) because the scattered inhabitants of the planetesimal disk, and main belt asteroids destabilized by planetary migration, would provide prodigious numbers of impactors in the inner solar system (Levison et al. 2001; Gomes et al. 2005).

Assuming that the historical brightness of the zodiacal cloud was proportional to the number of primitive objects that were scattered into the inner solar system on JFC-like orbits, we can estimate how it changed over time. In the pre-LHB stage in the Nice model, the leakage rate from the planetesimal disk beyond 15 AU was likely not significant relative to that at LHB. We thus expect that the MIR emission from the inner zodiacal cloud at $R < 5$ AU should have been relatively faint, except if a massive population of particles was sustained by collisions in the pre-LHB asteroid belt. Here, we focus on the LHB and post-LHB stages.

According to Wyatt et al. (2007), the asteroidal debris disk is expected to decay by orders of magnitude from the time of Jupiter's formation, which marked the start of the fragmentation-dominated regime in the asteroid belt (e.g., Bottke et al. 2005), to LHB. It thus seems unlikely that a massive population of debris could be sustained over 700 Myr by the collisional grinding of main belt asteroids. Instead, it has been suggested that the collisional grinding in the massive trans-planetary disk at $R > 15$ AU should have produced strong MIR emission peaking at ∼100 μm (Booth et al. 2009, hereafter B09). Being more distant the trans-planetary disk probably decayed more slowly by collisions than the asteroid belt. Thus, in the pre-LHB stage, the Wien side of the trans-planetary disk emission may have exceeded the one from the inner zodiacal cloud down to ∼20 μm (B09).

During the LHB, as defined by the Nice model, large numbers of outer disk planetesimals were scattered into the inner solar system and the inner zodiacal cloud could have become orders of magnitude brighter than it is now. To estimate how bright it actually was, we used simulations of the Nice model from Nesvorný & Vokrouhlický (2009, hereafter NV09). NV09 numerically tracked the orbital evolution of four outer planets and 27,029 objects representing the outer planetesimal disk. The mass of the disk was set to be 35 Earth masses. In total, NV09 performed 90 different numerical integrations of the Nice model, only some of which ended with the correct orbits of the outer planets.

We used these successful simulations to determine the number of scattered objects with JFC-like orbits as a fraction of the total initial number of planetesimals in the trans-planetary disk. Figure 16 shows how this fraction changed over time in one of the NV09 successful simulations. Consistently with the estimated physical lifetime of modern JFCs (LD97), we assumed that the physical lifetime of planetesimals after reaching $q < 2.5$ AU for the first time was 10^4 yr. Objects past their physical lifetime did not contribute to the statistic.

Immediately after the planetary instability occurred in the Nice model, the estimated fraction of planetesimals having JFC-like orbits was $\approx 7 \times 10^{-5}$ (Figure 16). It then decayed to $\approx 10^{-6}$ at 50 Myr after the start of LHB. Even though the NV09 simulations gradually lose resolution at later times due to

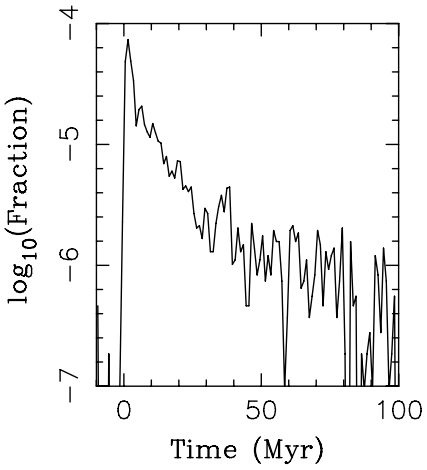

Figure 16. Number of objects on JFC-like orbits during LHB as a fraction of the total number of planetesimals in the pre-LHB trans-planetary planetesimal disk. The fraction was determined from the n22 simulation of the Nice model in NV09. We extracted all orbits from that simulation with perihelion distance $q < 2.5$ AU, orbital period $P < 20$ yr and assumed that the physical lifetime of these objects was 10^4 yr (LD97). We also used an averaging window of 1 My to improve the statistics. The total mass of the JFC population can be estimated from this plot by multiplying the fraction shown here by the initial mass of the trans-planetary disk. With the 35 Earth-mass disk, the peak in the mass of the JFC population at $t \approx 0$ corresponds to ∼0.3 lunar masses.

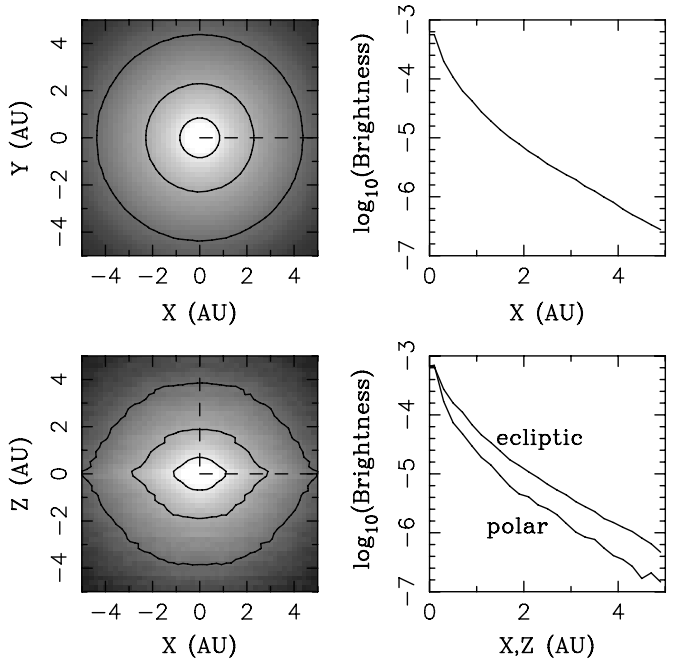

Figure 17. Zodiacal cloud brightness at 24 μm as seen by an observer at 10 pc. Two projections are shown: (top) polar view for an observer with $Z = 10$ pc and (bottom) side view of an observer in the ecliptic plane ($Y = 10$ pc). The three isophotes in each of the two left panels correspond to 5×10^{-4}, 5×10^{-5}, and 5×10^{-6} Jy AU^{-2} with 1 AU^2 at 10 pc corresponding to 0.01 arcsec^2. The shading scale is linear in $\log_{10}$ of brightness. The right panels show the brightness variation with the heliocentric distance along the cuts denoted by the dashed lines in the left panels. There are two lines in the bottom-right panel corresponding to the polar and ecliptic profiles. The brightness estimates shown here are not valid for heliocentric distance below ∼0.1 AU because of various limitations of our model (see, e.g., Section 3.2).

the insufficient number of tracked particles, we can still estimate that the fraction was $\sim 10^{-8}$ at 500 Myr, or about 3.4 Gyr ago in absolute chronology.

Charnoz et al. (2009) and Morbidelli et al. (2009) argued, using the crater record on Iapetus and the current size distribution of Jupiter's Trojans, that the total number of $D > 2$ km planetesimals in the pre-LHB trans-planetary disk was $\sim 10^{10}$–10^{12}. Using this value and Figure 16, we find that there were $\sim 7 \times 10^6$ JFCs with $D > 2$ km at time of the LHB peak, $t_{\rm LHB}$, and $\sim 10^5$ JFCs at $t_{\rm LHB} + 50$ Myr. These estimates are at least an order of magnitude uncertain mainly due to the poorly known size distribution of small planetesimals in the trans-planetary disk.

For comparison, Di Sisto et al. (2009) found, in a good agreement with the previous estimates of LD97, that there are ≈100 JFCs with $D > 2$ km and $q < 2.5$ AU in the current solar system (with about a factor of 50% uncertainty in this value). Therefore, if the inner zodiacal cloud brightness reflects variations in the size of the historical JFC population, we find that it has been $\sim 7 \times 10^4$ brighter at $t_{\rm LHB}$ and 2×10^3 brighter at $t_{\rm LHB} + 50$ Myr than it is now. This would correspond to the near-ecliptic 25 μm fluxes of 5×10^6 and 10^5 MJy sr^{-1}, respectively. These values largely exceed those expected from dust particles that were scattered from the trans-planetary disk (B09). Most of the action was apparently over by $t_{\rm LHB} + 500$ Myr, when our model suggests that the inner zodiacal cloud was only ∼10 times brighter than it is now.[7]

5.5. Distant Observations of the Zodiacal Cloud

Figure 17 shows how the present zodiacal cloud would look to a distant observer. If seen from the side, the brightest inner part of the zodiacal cloud has a disk-like shape with a ≈1.6 ratio between the ecliptic and polar dimensions. Similar shapes have been reported by Hahn et al. (2002) from Clementine observations of scattered light. At a larger distance from the Sun, the shape of the zodiacal cloud is oblate and shows cusps at the ecliptic. The axial ratio becomes ≈1.3 at $R = 5$ AU.

The radial brightness profiles in Figure 17 show a steep dimming of the zodiacal cloud with R. For $R < 1$ AU, a factor of ∼10 in brightness is lost per 1 AU. For $1 < R < 5$ AU, factor ∼10 is lost per 2 AU. These profiles are approximate because we ignored the effect of collisions in our model, which should be especially important for $R \lesssim 1$ AU. It is unclear how the shape of the zodiacal cloud would look for $R > 5$ AU because we did not model the contribution from KB dust.

Figure 18 shows the spectral energy distribution (SED) for distant unresolved observations of the zodiacal cloud. At a distance of 10 pc from the Sun, SED of the present inner zodiacal cloud is 1.4×10^{-4} Jy at 24 μm and 5.5×10^{-5} Jy at 70 μm, corresponding to the excesses over the Sun's photospheric emission at these wavelengths of about 3.4×10^{-4} and 1.1×10^{-3}, respectively. For comparison, the approximate 3σ excess detection limits of *Spitzer* telescope observations of Sun-like stars are 0.054 at 24 μm and 0.55 at 70 μm (Carpenter et al. 2009). The MIR emission of the present inner zodiacal cloud is therefore undetectable by distant unresolved observations with a *Spitzer*-class telescope. Specifically, the detectable emission levels are ≈160 and ≈500 larger at 24 and 70 μm, respectively, than those of the present inner zodiacal cloud.

When the flux is integrated over wavelengths, we find that the fractional bolometric luminosity of the inner zodiacal cloud, $L_{\rm ZODY}$, relative to that of the Sun, $L_\odot = 3.839 \times 10^{26}$ W, is

[7] These estimates should only be taken as a rough guideline to the historical zodiacal cloud brightness because the collisional environment in the dense disk of JFC particles at LHB must have been very different from the one existing today. It is therefore not exactly correct to assume that the historical brightness of the zodiacal cloud was strictly proportional to the population of JFCs.

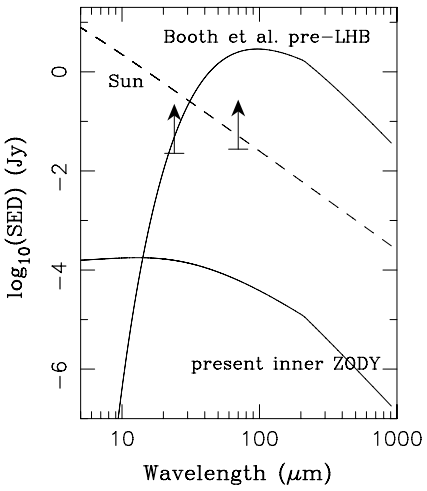

Figure 18. Spectral density distribution of the present inner zodiacal cloud as seen by an observer at distance 10 pc from the Sun. For reference, we also plot SED of the Sun and the pre-LHB trans-planetary disk as determined by Booth et al. (2009). The two arrows show the approximate 3σ detection limits of the *Spitzer* telescope at 24 and 70 μm (Carpenter et al. 2009; Wyatt 2008).

$L_{\rm ZODY}/L_{\odot} \sim 2 \times 10^{-7}$. This is a larger value than 10^{-8}–10^{-7} suggested by Dermott et al. (2002) and perhaps comparable to that of KB dust at $>$ 30 AU (Stern 1996). The effective blackbody temperature of the zodiacal cloud can be estimated from $T_{\rm eff} = 5100/\lambda_{\rm max}$, where $\lambda_{\rm max}$ is the wavelength of the SED maximum in microns. With $\lambda_{\rm max} = 18.5$ μm, this gives this gives $T_{\rm eff} = 276$ K.

5.6. MIR Excess During LHB

B09 studied how the MIR excess of the solar system debris disk varied with time. According to them, the main source of the pre-LHB MIR emission should have been the population of dust particles produced by collisions in the massive trans-planetary disk at $R > 20$ AU. In Figure 18, we show the model SED produced by the B09 trans-planetary disk. Being dominated by collisions (as opposed to PR drag regime; see Wyatt 2005), the trans-planetary particles are destroyed before they could evolve to $R < 20$ AU. The SED emission therefore peaks at longer wavelengths ($\approx$100 μm) than the SED of the present zodiacal cloud ($\approx$20 μm). Also, with $\sim$35 Earth masses in the pre-LHB trans-planetary disk, its estimated MIR emission is strong and produces excesses of $\sim$0.1 at 24 μm and $\sim$50 at 70 μm over Sun's photospheric emission at these wavelengths. These values are comparable to those of observed exozodiacal debris disks (B09).

The trans-planetary disk objects, including small dust particles, became scattered all around the solar system during LHB. This led to a significant depletion of the trans-planetary particle population which could not have been compensated by the collisional cascade because collisions became increasingly rare in the depleted disk. The MIR excess should have thus dropped by orders of magnitude within several hundred Myr after the LHB start. B09 estimated that the 24 μm excess of dust particles scattered from the trans-planetary disk should have dropped to $\sim 3 \times 10^{-5}$ at the present time. This is about an order-of-magnitude lower value than the 24 μm excess estimated by us for the current inner zodiacal cloud. Thus, there must have been a transition epoch some time after LHB when the 24 μm excess stopped being dominated by dust particles scattered from the trans-planetary disk and became dominated by particles produced by JFCs.

Figure 19 illustrates how the MIR emission of the inner zodiacal cloud should have varied with time during LHB. The size of the JFC population was estimated by using the methods described in Section 5.4. We then scaled up the MIR emission of the present inner zodiacal cloud by the appropriate factor (see Section 5.4). We found that the 24 μm excess reached $F_{\rm ZODY}/F_{\rm Sun}(24\ \mu{\rm m}) \sim 20$ at the LHB peak and stayed for about 100 Myr above the *Spitzer*'s 3σ detection limit. It dropped down to $\sim$10 times the value of the present zodiacal cloud at $t_{\rm LHB}$ + 500 Myr. We were unable to determine how this trend continues after $t_{\rm LHB}$ + 500 Myr because of the resolution issues with the NV09 simulations (Section 5.4). We expect that $F_{\rm ZODY}/F_{\rm Sun}(24\ \mu{\rm m})$ should have decayed by an additional factor of $\sim$10 from t_0 + 500 Myr to the present time.

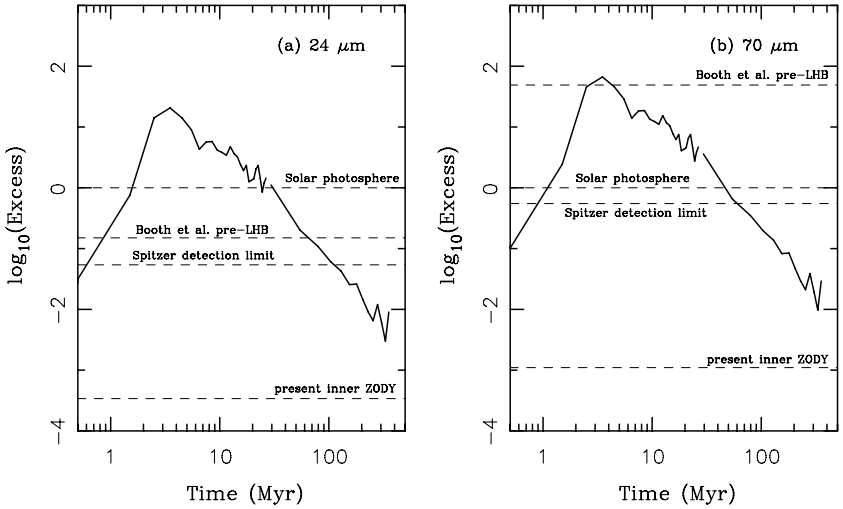

Figure 19. Expected variation of excesses at 24 μm (panel a) and 70 μm (b) during LHB (solid lines). To determine the excess values at different times during LHB, we used Figure 16 to estimate the number of objects that were scattered from the trans-planetary disk into the JFC-like orbits. By comparing this number to the present population of JFCs, a scale factor has been determined to represent the brightness increase of the inner zodiacal cloud over its current value. The discontinuity in the lines near $t = 30$ Myr appears because we changed the size of the averaging running window, δt. For $t < 30$ Myr, we used $\delta t = 1$ Myr; for $t > 30$ Myr, we used $\delta t = 50$ Myr. The large δt value is needed for $t > 30$ Myr to improve the statistics. For reference, the plot also shows the values predicted by Booth et al. (2009) for the pre-LHB trans-planetary disk, approximate *Spitzer* detection limits and present inner zodiacal cloud (dashed lines).

The 70 μm excess behaves similarly (Figure 19(b)). It reaches $F_{ZODY}/F_{Sun}(70\ \mu m) \sim 70$ at the LHB peak and decays at later times. Given the tighter detection limit of *Spitzer* at 70 μm, the 70 μm excess would remain detectable by *Spitzer* for 50 Myr, which is roughly half of the interval during which the 24 μm excess could be detected. Also, when these values are compared to the ones estimated by B09 for the pre-LHB trans-planetary disk, we find that the 70 μm excess expected for JFC particles at the LHB peak is comparable to that of the pre-LHB excess produced by collisions in the trans-planetary disk. We would thus expect that the solar system's LHB has not produced any significant increase of the 70 μm emission.

Conversely, the 24 μm excess raises a factor of ~100 above the B09 pre-LHB level, indicating that the solar system became significantly brighter during LHB at these shorter wavelengths. During LHB, the emission from JFC particles should have exceeded that of the scattered trans-planetary particles by ~20 (compare Figure 19(a) with Figure 5 in B09). Thus, the system does not need to have a significant cold dust disk at the same time as the hot dust disk to provide material for the hot disk. In fact, we find here that the hot disk can be fed by $D \gtrsim 1$ km objects, which have little total cross section area to be detected in the cold disk, but large mass to sustain the hot disk upon their disintegration at <10 AU (see Section 6). Since the decay rates of both populations after LHB should have been similar, their ratio should have remained roughly constant over time suggesting that the trans-planetary dust did not represent any significant contribution to the post-LHB emission of the zodiacal cloud at 24 μm.

5.7. Debris Disks

These results have interesting implications for our understanding of hot debris disks observed within 10 AU around mature stars (Trilling et al. 2008; Meyer et al. 2008; Carpenter et al. 2009; see also a review by Wyatt 2008). It has been argued that some of the observed brightest hot disks, such as HD 69830, HD 72905, HD 23514, η Corvi, and BD+20307, cannot be explained by assuming that they are produced by the collisional grinding of the local population of asteroids (Wyatt et al. 2007). Specifically, Wyatt et al. (2007) pointed out that the emission from a locally produced population of debris is expected to be much weaker than the observed emission because disks become depleted over time by collisions. This problem cannot be resolved by assuming a more massive initial population because the massive population would decay faster. Instead, Wyatt et al. proposed that the bright hot debris disks can be seen around stars with planetary systems that are undergoing the LHB instability akin to that invoked in the Nice model.

In Section 5.6, we estimated how the 24 μm and 70 μm excesses varied during the solar system's LHB. We found that the 24 μm excess should have rapidly risen by a large factor from the pre-LHB value and then gradually decayed. It would remain detectable by a *Spitzer*-class telescope for about 100 Myr after the LHB start, or ~2% of Sun's current age. The 24 μm excess reached values $\gtrsim$10 at LHB, which is comparable to those of the brightest known hot disks (Wyatt et al. 2007). Conversely, the solar system's LHB has not produced a significant increase of the 70 μm excess relative to the pre-LHB level. The 70 μm excess decayed after LHB and became undetectable by a *Spitzer*-class telescope after ~50 Myr. Thus, if the timing is right, debris disks may show the 24 μm excess but not the 70 μm excess. This could be relevant for systems such as HD 69830, which shows a large excess emission at 8–35 μm (Beichman et al. 2005), but lacks 70 μm emission, and HD 101259 (Trilling et al. 2008).

In a broader context, our study of the zodiacal cloud implies that (1) the populations of small debris particles can be generated by processes that do not involve, at least initially, disruptive collisions (see Section 6) and (2) observed hot dust around mature stars may not be produced from a population of objects that is native to <10 AU. Instead, in the solar system, most particles located within the orbit of Jupiter are fragments of planetesimals that formed at >15 AU. These icy objects are transported to <5 AU by gravitational encounters with the outer planets and disintegrate into small particles by disruptive splitting events (thought to occur due to processes such as the pressure buildup from heated volatiles or nucleus spin-up; see Section 6). If these processes are common around stars harboring planets, the collisional paradigm in which debris disks are explained by collisions of local populations of planetesimals (e.g., "exo-asteroids") may not be as universal as thought before.

5.8. LHB Accretion Rates

If our basic assumptions are correct, large quantities of dust should have been accreted by the Moon, Earth, and other terrestrial planets during LHB. For example, assuming 10^{14} g yr^{-1} mean accretion rate over 100 Myr we estimate that $\sim 10^{22}$ g of extraterrestrial material should have fallen on the Earth at the time of LHB (with ~50% of this mass accumulating in the first 10 Myr). This is ~50 times more mass than the quantity accumulated by the Earth at its current accretion rate over 4 Gyr. The Moon should have accreted about 2% of Earth's value during LHB, or $\sim 2\times10^{20}$ g in total over 100 Myr.

These estimates are at least 1 order of magnitude uncertain. They were obtained by scaling up the present accretion rates by the ratio between the estimated population of JFCs at LHB and their present number. The contribution from planetesimals larger than the largest presently observed JFCs was ignored. This contribution may have been important if most mass of the trans-planetary disk were in $D \gtrsim 20$ km planetesimals (Morbidelli et al. 2009). Assuming that *all* planetesimals reaching $q < 2.5$ AU during LHB became disrupted and dissolved into small particles, we estimate that up to $\sim 10^{24}$ g of this material could have been accreted by the Earth.[8]

In reality, significant mass losses must have occurred because many planetesimals or their large fragments were removed by Jupiter before they could fully disintegrate. Also, small dust grains could have been disrupted and blown away by the radiation pressure before they would reach 1 AU. The real mass accreted by the Earth during LHB is thus probably significantly lower than $\sim 10^{24}$ g. This also places an upper mass limit, $\sim 2\times10^{22}$ g, on the LHB accretion of dust particles by the Moon. For comparison, the mass of large impactors estimated from the number and size distribution of lunar basins is 6×10^{21} g (Hartmann et al. 2000). Thus, the total mass of carbonaceous dust deposited on the Moon during LHB could have been as low as ~1/30 of that of the large impactors, or up to 3 times larger. These larger values may be inconsistent with the lunar geological record.

The LHB is of fundamental interest in studies of the origin of life because it immediately precedes the oldest evidence for a biosphere (Awramik et al. 1983; Schidlowski 1988; Mojzsis

[8] This estimate uses the 35 Earth-mass disk, 20% fraction reaching $q < 2.5$ AU, 10^{-4} collision probability with the Earth, and 50% of dust in comets.

et al. 1996). The significance of our results in this context is that JFC dust grains can bring in unaltered primitive material from the outer solar system. They could potentially be the source of the earliest organic material that gave rise to life on Earth (e.g., Jenniskens 2001; Jenniskens et al. 2004). Note that the high abundance of organics is a defining property of comets (Bockelée-Morvan et al. 2004). Both MMs and Wild-2 particles contain two important classes of organic molecules: amino acids and PAHs (Sandford et al. 2006; Engrand & Maurette 1998).

6. COMET DISRUPTIONS

Today, ≈3.8 Gyr after LHB, the steady flux of JFCs from the outer solar system is keeping the zodiacal cloud at roughly constant brightness. We find from our numerical simulations that the mean dynamical lifetime of $D = 200$ μm JFC particles is 10^6 yr. Thus, to keep the zodiacal cloud at constant brightness, a continuous input of $\sim 3.4 \times 10^{19}/10^6 = 3.4 \times 10^{13}$ g yr^{-1}, or roughly 1100 kg s^{-1} is required in our model. This estimate is robust because it is insensitive to the assumed ρ and D values of particles (i.e., lighter particles have shorter dynamical lifetimes). It neglects, however, the loss of particles due to the disruptive collisions. The real input rate should therefore be slightly larger, probably somewhere in the 1000–1500 kg s^{-1} range. This is only slightly larger than 600–1000 kg s^{-1} suggested by Leinert et al. (1983) from modeling of the Helios 1 and 2 data.

For comparison, Reach et al. (2007) suggested from the *Spitzer* survey of cometary debris trails that the total meteoroid input from active short-period comets is ∼300 kg s^{-1} (see also Lisse 2002). This is ∼3–5 times lower value than what would be required, according to our estimate, to keep the zodiacal cloud brightness at constant brightness. While some of the uncertainties in our model and the Reach et al. results may be blamed for this discrepancy, we believe that this comparison may indicate that the trails of active comets represent only a fraction of the real mass loss in comets. In fact, it has been suggested that the main mass-loss mechanism in comets is their spontaneous (i.e., non-tidal) disruptions followed up by the progressive splitting of comet components into smaller fragments (e.g., Weissman 1980; also see Chen & Jewitt 1994; Boehnhardt 2004; Fernández 2005; Jenniskens 2006).

The best documented case of comet fragmentation is that of sungrazers. These are small comet fragments that are detected because they pass very close to the Sun and are seen in backscattered light by solar telescopes (Sekanina & Chodas 2004, 2005). Specific cases of JFCs that were observed to spontaneously split or break up into two or more components include 51P/Harrington, 73P/Schwassmann-Wachmann 3, and 141P/Machholz 2 (Fernández 2005). Observations of these events show that there does not seem to be a correlation between the splitting event and orbital phase of the parent object, which provides motivation for how particles were released from JFCs in our model (Section 3.1).

Several fragmentation mechanisms may explain the splitting of cometary nuclei: (1) rotational splitting when the centrifugal force exceeds the nucleus' self-gravity and material strength, (2) splitting by thermal stress produced by the variable distance to the Sun, and (3) splitting by internal gas pressure caused by sublimation of subsurface pockets of volatile ices (e.g., CO). It has not been possible find the main culprit so far. Plausibly, several different mechanisms contribute and more observational constraints will be needed to distinguish between them. See Weissman (1980) and Boehnhardt (2004) for a discussion.

Fernández (2005) compiled a list of 12 observed split JFCs. He found that the chance of JFC undergoing an observed splitting event is ≈1% per orbital period. This should be taken as a lower limit on the actual number of splitting events because many are undetected. For example, Chen & Jewitt (1994) estimated that a comet has a ∼1% chance to split per yr. Thus, over its active lifespan of about 10^4 yr (LD97), a typical JFC would undergo as many as ∼100 splitting events. These events may lead to the situation where the comet nucleus becomes completely dissolved into small particles. *The zodiacal cloud may thus plausibly be sustained by disintegrating JFCs.*

Our order-of-magnitude estimate supports this possibility because JFCs evolving into the inner solar system represent a continuous input of mass that is apparently large enough to compensate for the zodiacal cloud mass loss. Moreover, we found no evidence in this work for $t_{\rm JFC}$ values larger than the physical lifetime of active comets estimated in LD97. Most JFC comets should therefore be dissolved on timescales comparable to their active lifetime.

Using the size distribution of JFCs from Tancredi et al. (2006), we find that the total mass of JFCs with radius $0.1 < s < 10$ km and $q < 2.5$ AU is 3.9×10^{14} g. Assuming that this mass is injected into the zodiacal cloud every 10^4 yr (LD97), we find the total mass input of 12,000 kg s^{-1}. This is significantly larger than the mass input required to maintain the zodiacal cloud in a steady state (1000–1500 kg s^{-1}), possibly suggesting a ∼10% yield of the disintegration process. Note, for example, that some JFCs or their large fragments can be removed (e.g., impact planets or leave the solar system) before they could fully disintegrate. Also, icy particles released by comets sublimate at $R < 5$ AU and do not contribute to the inner zodiacal cloud.

Di Sisto et al. (2009) determined the physical lifetime of JFCs to be ∼3 times shorter than LD97. Using the Di Sisto et al. estimate, we find that the JFC population should require the mass input of 35,000 kg s^{-1}. The yield of the disintegration process may thus be as low as ∼3%. For comparison, Di Sisto et al. found the following fractions of JFCs that are completely dissolved by splitting events: 51% for radius $s = 1$ km, 13% for $s = 5$ km, and 8% for $s = 10$ km.

The initial size distribution of particles resulting from the splitting process is uncertain, but meteor showers from freshly ejected dust trails, such as Phoenicids, indicate that the distribution should be fairly flat with most mass in mm to cm size grains. This initial size distribution is modified by collisions as JFC particles decouple from Jupiter and drift to lower R where collisions are more common. As discussed in Section 4.2, the collisional effects explain why $D \approx 100$ μm provide the best fit to the *IRAS* data, because these intermediate-size particles have longest lifespans (e.g., Grün et al. 1985; Dermott et al. 2001).

Additional evidence that disruptions/splitting events of JFCs may dominate the population of interplanetary particles in short-period orbits comes from observations and modeling of the meteor showers. Specifically, it has been established that most meteor streams were produced by recent (<few thousand years ago) comet disruptions (see Jenniskens 2008 for a review). For example, 1956 Phoenicids and near-Earth object 2003 WY25 are most likely fragments produced by a breakup of D 1819 W1 (Blanpain) (Jenniskens & Lyytinen 2005; Watanabe et al. 2006). In addition to 2P/Encke, there are other known comet fragments moving in the Taurid stream (Jenniskens 2006), also pointing to a disruption event. Geminids, Phaeton, and 2005 UD can also be linked to the common parent body (Jenniskens 2006; Ohtsuka 2005; Jewitt & Hsieh 2006). The type of disintegration

that produced these large fragments and meteoroid streams is probably like that of the 1995 breakup of 73P/Schwassmann-Wachmann 3, which will cause a shower of tau-Herculidis in 2022.

The meteoroid streams that were associated with comet disruptions are much stronger than the meteoroid streams produced by active JFCs. Thus, the strong meteoroid streams may represent an important link between JFCs and the zodiacal cloud. They should become increasingly more dispersed due to effects of planetary perturbations. Eventually, the particles should be well mixed in orbital space, producing both the sporadic meteoroid complex and zodiacal cloud. Notably, the time-integrated flux of visual meteors at Earth is dominated by about a factor of ∼10 by sporadics (Jones & Brown 1993).

7. COMPARISON WITH PREVIOUS WORK

The origin and evolution of the zodiacal cloud has been the subject of numerous studies. For example, Liou et al. (1995) suggested, based on modeling in many ways similar to our own, that the observed shape of the zodiacal cloud can be accounted for by a combination of ∼1/4–1/3 of asteroid dust and ∼2/3–3/4 cometary dust. We found a much larger JFC contribution and much smaller asteroid contribution in this work. The cause of this difference is unknown. Possibly, it stems from some of the approximations used by Liou et al. (1995). For example, they used particles from comet 2P/Encke to represent the whole population of particles released by JFCs. This comet has a special orbit ($a = 2.22$ AU and $q = 0.33$ AU) that is not representative for the JFC population as a whole.

Different constraints on the origin of the zodiacal cloud have been obtained from modeling the asteroid dust bands. For example, Dermott et al. (1994a) suggested that the particles originating in the main asteroid belt supply ∼1/3 of the zodiacal cloud, while NVBS06 estimated the contribution of asteroidal particles to be <10%. Our results presented in Section 4 are more in line with the NVBS06 estimate. Specifically, we found that a $\gtrsim$20% asteroid contribution to the *near-ecliptic* MIR fluxes can be ruled out from *IRAS* observations. If correct, this limits the asteroid contribution to the *overall* cross section of the zodiacal cloud to a sub-10% level.

Hahn et al. (2002) used Clementine observations of the zodiacal cloud at optical wavelengths and arguments based on the inclination distribution of small bodies in the solar system to argue that at least ≈90% of the zodiacal cloud cross section enclosed by a 1 AU-radius sphere around the Sun is of cometary origin. They also found that ≈45% optical cross section at 1 AU comes from JFCs and/or asteroids. Unfortunately, a distinction between JFC and asteroid dust could not have been made because Hahn et al. used an approximate model for the interplanetary dust complex. According to our model, the contribution of JFC is much larger than the one found by Hahn et al. (2002). Thus, while we agree with the general conclusion of Hahn et al. about the predominant comet dust population, our results are more specifically pointing out JFCs as the main source.

8. ORIGIN OF PARTICLE POPULATIONS BEYOND JUPITER

Our findings are in broad agreement with the results obtained from dust detectors onboard spacecrafts. For example, Altobelli et al. (2007) identified two main groups of particles in the Cassini's Cosmic Dust Analyzer data set (measurements in the ecliptic plane between Jupiter and Saturn). The first group of impactors consists of particles on bound and prograde orbits, most probably having moderately eccentric and moderately inclined orbits. These grains are consistent with JFCs. Impactors of the second group were identified as small interstellar dust particles, perhaps including a minority of beta-meteoroids.

Landgraf et al. (2002) reported results from the dust experiments onboard the Pioneer 10 and 11 spacecrafts. They found that the spatial number density of $\gtrsim$10 μm particles at the ecliptic is only slowly declining with heliocentric distance in the 3–18 AU range. Specifically, there is no obvious gap beyond 4 AU, expected if asteroidal particles were the dominant source of dust in the inner solar system (Figure 13).

The nearly constant spatial density of the circumsolar dust beyond 5 AU is puzzling. To explain it, Landgraf et al. (2002) proposed that particle populations beyond Saturn are be dominated by dust produced in KB collisions (see also Moro-Martín & Malhotra 2003). The observed radial density profile beyond 5 AU is produced in their model by combining the contributions from KB particles, whose spatial density raises with R, and cometary particles, whose density declines with R. Indeed, the spatial density of JFC particles that we obtain from our model rather steeply declines with R at $R > 5$ AU. Thus, the Kuiper Belt dust may indeed be needed to explain Pioneer measurements. (A possible caveat of these considerations is that the impact rates measured by Pioneer 1 and 2 should be mainly those of ∼10 μm particles, while the dominant size of particles in the inner zodiacal cloud is ∼100–200 μm.)

An alternative possibility is that we do not correctly determine the distribution of JFC grains for $R > 5$ AU in our model. This alternative is attractive for the following reasons.

If the trans-Neptunian population is in the collisional equilibrium for $D < 1$ km, most mass should be contained in comet-size and larger bodies rather than in $D < 1000$ μm grains. Since the transfer of this material to the Jupiter-crossing orbit is size independent (driven mainly by the encounters to outer planets), JFCs must represent much more mass than their grain-sized orbital counterparts. Thus, assuming that JFCs can be efficiently dissolved by splitting events, the dust population they produce should be much more important than the one evolving from the Kuiper Belt in the form of dust grains.

Di Sisto et al. (2009) found a very high splitting rate of JFCs with only a shallow dependence on their perihelion distance ($\propto q^{\alpha}$ with $\alpha \sim -0.5$). Thus, if JFCs can be efficiently dissolved at large q, the radial distribution of JFC dust should significantly differ from the one obtained here (see Section 3.1 for our assumptions). The spatial density of JFCs is proportional to R^{γ} with $\gamma \sim 0.5$ (LD97; Di Sisto et al. 2009). Since $|\alpha| \sim \gamma$, the number of splitting events, and therefore the number of generated JFC particles, should be roughly independent of R. It might thus be plausible to explain the Pioneer measurements with JFC particles alone, i.e., without a major contribution from KB particles. A detail investigation into these issues goes beyond the scope of this paper.

9. SUMMARY

We developed models for various source populations of asteroid and cometary dust particles. These models were based on our current understanding of the origin and evolution of asteroids, JFC, HTC, and OCC. We launched submillimeter particles from these populations and tracked their orbital evolution due to radiation pressure, PR drag, and planetary perturbations. The thermal MIR emission from the synthetic particle distributions

were determined and the results were compared to *IRAS* observations.

The main goal of this modeling effort was to determine the relative contribution of asteroid and cometary material to the zodiacal cloud. We found that asteroidal particles produced by the main belt collisions cannot produce the zodiacal cloud emission at large ecliptic latitudes simply because the main belt asteroids have generally small orbital inclinations, and because the orbital effects of planetary encounters and secular resonances at $a \lesssim 2$ AU are not powerful enough to spread the asteroid dust to very large orbital inclinations. Therefore, most MIR emission from particles produced in the asteroid belt is confined to within $\sim 30^\circ$ of the ecliptic (Figure 6). Conversely, the zodiacal cloud has a broad latitudinal distribution so that strong thermal emission is observed even in the direction to the ecliptic poles (Figure 2).

We found that JFC particles are scattered by Jupiter before they are able to orbitally decouple from the planet and drift down to 1 AU. Therefore, the inclination distribution of JFC particles is broader than that of their source comets. This explains why JFC particles produce such a good fit to the broad latitudinal distribution of fluxes observed by *IRAS*.

Based on the results discussed in Section 4, we proposed that $\gtrsim$90% of the zodiacal cloud emission at MIR wavelengths comes from dust grains released by JFCs, and $\lesssim$10% comes from the OCCs and/or asteroid collisions. We argued that disruptions/splitting events of JFCs are more likely to produce the bulk of observed dust in the inner solar system than the normal JFC activity. The relative importance of JFC and Kuiper Belt particles beyond Jupiter has yet to be established.

Using our model results, we estimated the total cross section area and mass of particles in the zodiacal cloud, current and historical accretion rates of dust by planets and the Moon, and discussed the implications of our work for studies of MMs and debris disks. We found that JFC particles should dominate the terrestrial accretion rate of micrometeoroids. This may explain why most antarctic MMs have primitive carbonaceous composition. If the spontaneous comet disruptions are also common in the hot exozodiacal debris disks, the collisional paradigm used to explain their properties may not be as universal as thought before.

This work was supported by the NASA Planetary Geology and Geophysics and Planetary Astronomy programs. The work of D.V. was partially supported by the Czech Grant Agency (grant 205/08/0064) and the Research Program MSM0021620860 of the Czech Ministry of Education. We thank C. M. Lisse, A. Morbidelli, L. Dones, W. T. Reach, and two anonymous referees for their insightful comments on the manuscript.

REFERENCES

Altobelli, N., Dikarev, V., Kempf, S., Srama, R., Helfert, S., Moragas-Klostermeyer, G., Roy, M., & Grün, E. 2007, J. Geophys. Res. (Space Phys.), 112, 7105

Awramik, S. M., Schopf, J. W., & Walter, M. R. 1983, Precambrian Res., 20, 357

Beichman, C. A., et al. 2005, ApJ, 626, 1061

Bertotti, B., Farinella, P., & Vokrouhlický, D. 2003, Physics of the Solar System (Dordrecht: Kluwer)

Bhattacharya, B., & Reach, W. T. 2004, BAAS, 36, 1432

Bockelée-Morvan, D., Crovisier, J., Mumma, M. J., & Weaver, H. A. 2004, in Comets II, ed. M. C. Festou, H. U. Keller, & H. A. Weaver (Tucson, AZ: Univ. Arizona Press), 391

Boehnhardt, H. 2004, in Comets II, ed. M. C. Festou, H. U. Keller, & H. A. Weaver (Tucson, AZ: Univ. Arizona Press), 301

Booth, M., Wyatt, M. C., Morbidelli, A., Moro-Martín, A., & Levison, H. F. 2009 (B09), MNRAS, 1141

Bottke, W. F., Durda, D. D., Nesvorný, D., Jedicke, R., Morbidelli, A., Vokrouhlický, D., & Levison, H. 2005, Icarus, 175, 111

Bowell, E., Muinonen, K., & Wasserman, L. H. 1994, in IAU Symp. 160, Asteroids, Comets, Meteors, ed. A. Milani, M. D. Martino, & A. Cellino (Dordrecht: Kluwer), 477

Brown, P. G., & Campbell-Brown, M. D. 2003, BAAS, 35, 987

Brown, P. G., & Jones, J. 1999, in Proc. Int. Conf. on Meteroids, Tatranska Lomnica, Slovakia, ed. W. J. Baggaley & V. Porubčan (Tatranska Lomnica: Astronomical Institute of the Slovak Academy of Sciences), 159

Burns, J. A., Lamy, P. L., & Soter, S. 1979, Icarus, 40, 1

Carpenter, J. M., et al. 2009, ApJS, 181, 197

Ceplecha, Z., Borovička, J., Elford, W. G., Revelle, D. O., Hawkes, R. L., Porubčan, V., & Šimek, M. 1998, Space Sci. Rev., 84, 327

Chapman, C. R., Cohen, B. A., & Grinspoon, D. H. 2007, Icarus, 189, 233

Charnoz, S., Morbidelli, A., Dones, L., & Salmon, J. 2009, Icarus, 199, 413

Chen, J., & Jewitt, D. 1994, Icarus, 108, 265

Clarke, D., Matthews, S. A., Mundell, C. G., & Weir, A. S. 1996, , A&A, 308, 273

Dermott, S. F., Durda, D. D., Gustafson, B. A. S., Jayaraman, S., Liou, J. C., & Xu, Y. L. 1994a, in IAU Symp., Asteroids, Comets, Meteors, ed. A. Milani et al. (Dordrecht: Kluwer), 127

Dermott, S. F., Grogan, K., Durda, D. D., Jayaraman, S., Kehoe, T. J. J., Kortenkamp, S. J., & Wyatt, M. C. 2001, in Interplanetary Dust, ed. E. Grün, B. S. Gustafson, S. Dermott, & H. Fechtig (Berlin: Springer), 569

Dermott, S. F., Grogan, K., Jayaraman, S., & Xu, Y. L. 1995, , BAAS, 27, 1084

Dermott, S. F., Jayaraman, S., Xu, Y. L., Gustafson, B. Å. S., & Liou, J. C. 1994b, Nature, 369, 719

Dermott, S. F., Kehoe, T. J. J., Durda, D. D., Grogan, K., & Nesvorný, D. 2002, in Asteroids, Comets, and Meteors, ed. B. Warmbein (Noordwijk: ESA), 319

Dermott, S. F., Nicholson, P. D., Burns, J. A., & Houck, J. R. 1984, Nature, 312, 505

Dermott, S. F., Nicholson, P. D., Kim, Y., Wolven, B., & Tedesco, E. F. 1988, in Comets to Cosmology, ed. A. Lawrence (Berlin: Springer), 3

Di Sisto, R. P., Fernández, J. A., & Brunini, A. 2009, Icarus, 203, 140

Dikarev, V., Grün, E., Baggaley, J., Galligan, D., Landgraf, M., & Jehn, R. 2004, 35th COSPAR Scientific Assembly, The New ESA Meteoroid Model, Paris, France, 575

Divine, N. 1993, J. Geophys. Res., 98, 17029

Dobrica, E., Engrand, C., Duprat, J., Gounelle, M., Leroux, H., Quirico, E., & Rouzaud, J.-N. 2010, MAPS, 44, 1643

Dones, L., Weissman, P. R., Levison, H. F., & Duncan, M. J. 2004, in Comets II, ed. M. C. Festou, H. U. Keller, & H. A. Weaver (Tucson, AZ: Univ. Arizona Press), 153

Dumont, R., & Levasseur-Regourd, A.-C. 1988, A&A, 191, 154

Durda, D. D., & Dermott, S. F. 1997, Icarus, 130, 140

Engrand, C., & Maurette, M. 1998, Meteorit. Planet. Sci., 33, 565

Farley, K. A., Montanari, A., Shoemaker, E. M., & Shoemaker, C. S. 1998, Science, 280, 1250

Farley, K. A., Vokrouhlický, D., Bottke, W. F., & Nesvorný, D. 2006, Nature, 439, 295

Fernández, J. A. 2005, in Comets: Nature, Dynamics, Origin and their Cosmogenic Relevance (Dordrecht, The Netherlands: Springer), 249

Fixsen, D. J., & Dwek, E. 2002, ApJ, 578, 1009

Flynn, G. J. 1995, Meteoritics, 30, 504

Francis, P. J. 2005, ApJ, 635, 1348

Gaidos, E. J. 1999, ApJ, 510, L131

Galligan, D. P., & Baggaley, W. J. 2004, MNRAS, 353, 422

Genge, M. J. 2006, Meteorit. Planet. Sci. Suppl., 41, 5070

Gladman, B. J., et al. 2009, Icarus, 202, 104

Gomes, R., Levison, H. F., Tsiganis, K., & Morbidelli, A. 2005, Nature, 435, 466

Good, J. C., Gautier, T. N., & Hauser, M. G. 1986, Adv. Space Res., 6, 83

Greaves, J. S., Wyatt, M. C., Holland, W. S., & Dent, W. R. F. 2004, MNRAS, 351, L54

Grogan, K., Dermott, S. F., & Durda, D. D. 2001, Icarus, 152, 251

Grogan, K., Dermott, S. F., Jayaraman, S., & Xu, Y. L. 1997, , Planet. Space Sci., 45, 1657

Grün, E., Zook, H. A., Fechtig, H., & Giese, R. H. 1985, Icarus, 62, 244

Gustafson, B. A. S. 1994, Ann. Rev. Earth Planet. Sci., 22, 553

Gustafson, B. A. S., Greenberg, J. M., Kolokolova, L., Xu, Y., & Stognienko, R. 2001, in Interplanetary Dust, ed. E. Grün, B. S. Gustafson, S. Dermott, & H. Fechtig (Berlin: Springer), 509

Hahn, J. M., Zook, H. A., Cooper, B., & Sunkara, B. 2002, Icarus, 158, 360

Hartmann, W. K., Ryder, G., Dones, L., & Grinspoon, D. 2000, in Origin of the Earth and Moon, ed. R. M. Canup, et al. (Tucson, AZ: Univ. Arizona Press), 493
Hauser, M. G., et al. 1984, ApJ, 278, L15
Hirschi, D. C., & Beard, D. B. 1987, Planet. Space Sci., 35, 1021
Hong, S. S. 1985, A&A, 146, 67
Hunt, S. M., Oppenheim, M., Close, S., Brown, P. G., McKeen, F., & Minardi, M. 2004, Icarus, 168, 34
Ipatov , Sergei, I., Kutyrev, A. S., Madsen, G. J., Mather, J. C., Moseley, S. H., & Reynolds, R. J. 2008, Icarus, 194, 769
Ishiguro, M., Nakamura, R., Fujii, Y., Morishige, K., Yano, H., Yasuda, H., Yokogawa, S., & Mukai, T. 1999, ApJ, 511, 432
Jacchia, L. G., & Whipple, F. L. 1961, Smithsonian Contrib. Astrophys., 4, 97
Jedicke, R., & Metcalfe, T. S. 1998, , Icarus, 131, 245
Jenniskens, P. 2001, in Proc. Meteoroids 2001 Conference, ed. B. Warmbein (ESA SP-495; Noordwijk: ESA), 247
Jenniskens, P. 2006, in Meteor Showers and their Parent Comets, ed. P. Jenniskens (Cambridge: Cambridge Univ. Press)
Jenniskens, P. 2008, Earth Moon Planets, 102, 505
Jenniskens, P., & Lyytinen, E. 2005, AJ, 130, 1286
Jenniskens, P., Schaller, E. L., Laux, C. O., Wilson, M. A., Schmidt, G., & Rairden, R. L. 2004, Astrobiology, 4, 67
Jewitt, D., & Hsieh, H. 2006, AJ, 132, 1624
Jones, J., & Brown, P. 1993, MNRAS, 265, 524
Joswiak, D. J., Brownlee, D. E., Pepin, R. O., & Schlutter, D. J. 2007, in Proc. Dust in Planetary Systems, Kauai Hawaii, USA (ESA SP-643), ed. H. Krueger & A. Graps (Noordwijk: ESA), 141
Kelsall, T., et al. 1998, ApJ, 508, 44
Kessler, D. J. 1981, Icarus, 48, 39
Kniessel, B., & Mann, I. 1991, in Origin and Evolution of Interplanetary Dust, ed. A. C. Levasseur-Regourd & H. Hasegawa (Dordrecth: Kluwer), 139
Kortenkamp, S. J., & Dermott, S. F. 1998, Icarus, 135, 469
Landgraf, M., Liou, J.-C., Zook, H. A., & Grün, E. 2002, AJ, 123, 2857
Lauretta, D. S., & McSween, H. Y., Jr. 2008, Meteorites and Early Solar System 2 (Tucson, AZ: Arizona Univ. Press)
Leinert, Ch., Ábrahám, P., Acosta-Pulido, J., Lemke, D., & Siebenmorgen, R. 2002, A&A, 393, 1073
Leinert, C., Roser, S., & Buitrago, J. 1983, A&A, 118, 345
Levasseur-Regourd, A. C., Mann, I., Dumont, R., & Hanner, M. S. 2001, in Interplanetary Dust, ed. E. Gruen, B. A. S. Gustafson, S. F. Dermott, & H. Fechtig (Berlin: Springer), 57
Levison, H. F., Bottke, W. F., Gounelle, M., Morbidelli, A., Nesvorný, D., & Tsiganis, K. 2009, Nature, 460, 364
Levison, H. F., Dones, L., Chapman, C. R., Stern, S. A., Duncan, M. J., & Zahnle, K. 2001, Icarus, 151, 286
Levison, H. F., & Duncan, M. J. 1994, Icarus, 108, 18
Levison, H. F., & Duncan, M. J. 1997 (LD97), Icarus, 127, 13
Levison, H. F., Duncan, M. J., Dones, L., & Gladman, B. J. 2006, Icarus, 184, 619
Levison, H. F., Morbidelli, A., Vanlaerhoven, C., Gomes, R., & Tsiganis, K. 2008, Icarus, 196, 258
Liou, J. C., Dermott, S. F., & Xu, Y. L. 1995, Planet. Space Sci., 43, 717
Lisse, C. 2002, Earth Moon Planets, 90, 497
Lisse, C. M., et al. 2006, Science, 313, 635
Love, S. G., & Brownlee, D. E. 1993, Science, 262, 550
Love, S. G., Joswiak, D. J., & Brownlee, D. E. 1994, Icarus, 111, 227
Low, F. J., et al. 1984, ApJ, 278, L19
Maris, M., Burigana, C., & Fogliani, S. 2006, A&A, 452, 685
Mathews, J. D., Janches, D., Meisel, D. D., & Zhou, Q.-H. 2001, Geophys. Res. Lett., 28, 1929
McDonnell, J. A. M., & Gardner, D. J. 1998, Icarus, 133, 25
Meyer, M. R., et al. 2008, ApJ, 673, L181
Mojzsis, S. J., Arrhenius, G., McKeegan, K. D., Harrison, T. M., Nutman, A. P., & Friend, C. R. L. 1996, Nature, 384, 55
Morbidelli, A., Levison, H. F., Bottke, W. F., Dones, L., & Nesvorný, D. 2009, Icarus, 202, 310
Morbidelli, A., Levison, H. F., Tsiganis, K., & Gomes, R. 2005, Nature, 435, 462
Moro-Martín, A., & Malhotra, R. 2003, AJ, 125, 2255
Mueller, T. G., Abraham, P., & Crovisier, J. 2005, Space Sci. Rev., 119, 141
Mukai, T., & Mann, I. 1993, A&A, 271, 530
Nesvorný, D., Bottke, W. F., Levison, H. F., & Dones, L. 2003, ApJ, 591, 486
Nesvorný, D., Bottke, W. F., Vokrouhlický, D., Sykes, M., Lien, D. J., & Stansberry, J. 2008, ApJ, 679, L143
Nesvorný, D., & Vokrouhlický, D. 2009 (NV09), AJ, 137, 5003
Nesvorný, D., Vokrouhlický, D., Bottke, W. F., & Sykes, M. 2006 (NVBS06), Icarus, 181, 107
Nesvorný, D., Vokrouhlický, D., & Morbidelli, A. 2007, AJ, 133, 1962
Ohtsuka, K. 2005, 2005 UD and the Daytime Sextantids, CBET 283 (Cambridge, MA: Minor Planet Center)
Öpik, E. J. 1951, Proc. R. Irish Acad., 54, 165
Press, W. H., Teukolsky, S. A., Vetterling, W. T., & Flannery, B. P. 1992, Numerical Recipes in FORTRAN. The Art of Scientific Computing (2nd ed.; Cambridge: Cambridge Univ. Press), c1992
Price, S. D., Noah, P. V., Mizuno, D., Walker, R. G., & Jayaraman, S. 2003, AJ, 125, 962
Reach, W. T., Franz, B. A., & Weiland, J. L. 1997, Icarus, 127, 461
Reach, W. T., Kelley, M. S., & Sykes, M. V. 2007, Icarus, 191, 298
Reach, W. T., Morris, P., Boulanger, F., & Okumura, K. 2003, Icarus, 164, 384
Reach, W. T., et al. 1995, Nature, 374, 521
Reach, W. T., et al. 1996, A&A, 315, L381
Renard, J. B., Levasseur-Regourd, A. C., & Dumont, R. 1995, A&A, 304, 602
Reynolds, R. J., Madsen, G. J., & Moseley, S. H. 2004, ApJ, 612, 1206
Sandford, S. A., et al. 2006, Science, 314, 1720
Schidlowski, M. 1988, Nature, 333, 313
Sekanina, Z., & Chodas, P. W. 2004, ApJ, 607, 620
Sekanina, Z., & Chodas, P. W. 2005, ApJS, 161, 551
Staubach, P., Grün, E., & Jehn, R. 1997, Adv. Space Res., 19, 301
Staubach, P., Grün, E., & Matney, M. J. 2001, in Interplanetary Dust, ed. E. Grün, B. S. Gustafson, S. Dermott, & H. Fechtig (Berlin: Springer), 347
Stern, S. A. 1996, AJ, 112, 1203
Sykes, M. V. 1990, Icarus, 85, 267
Sykes, M. V., & Greenberg, R. 1986, Icarus, 65, 51
Sykes, M. V., Grün, E., Reach, W. T., & Jenniskens, P. 2004, in Comets II, ed. M. C. Festou, H. U. Keller, & H. A. Weaver (Tucson, AZ: Univ. Arizona Press), 677
Tancredi, G., Fernández, J. A., Rickman, H., & Licandro, J. 2006, Icarus, 182, 527
Taylor, A. D. 1995, Icarus, 116, 154
Taylor, A. D., & Elford, W. G. 1998, Earth Planets Space, 50, 569
Taylor, S., Lever, J. H., & Harvey, R. P. 1996, Meteorit. Planet. Science, 31, A140
Tera, F., Papanastassiou, D. A., & Wasserburg, G. J. 1974, Earth Planetary Sci. Lett., 22, 1
Trilling, D. E., et al. 2008, ApJ, 674, 1086
Tsiganis, K., Gomes, R., Morbidelli, A., & Levison, H. F. 2005, Nature, 435, 459
Vokrouhlický, D., Nesvorný, D., & Bottke, W. F. 2008, ApJ, 672, 696
Watanabe, J.-I., Sato, M., & Kasuga, T. 2006, Astron. Her., 99, 629
Weissman, P. R. 1980, A&A, 85, 191
Wetherill, G. W. 1967, J. Geophys. Res., 72, 2429
Wiegert, P., & Tremaine, S. 1999, Icarus, 137, 84
Wiegert, P., Vaubaillon, J., & Campbell-Brown, M. 2009, Icarus, 201, 295
Wisdom, J., & Holman, M. 1991, AJ, 102, 1528
Wyatt, M. C. 2005, A&A, 433, 1007
Wyatt, M. C. 2008, ARA&A, 46, 339
Wyatt, M. C., Smith, R., Greaves, J. S., Beichman, C. A., Bryden, G., & Lisse, C. M. 2007, ApJ, 658, 569
Younger, J. P., Reid, I. M., Vincent, R. A., Holdsworth, D. A., & Murphy, D. J. 2009, MNRAS, 398, 350